Methods for the estimation of depth-resolved attenuation in OCT

by
Mehar Rehill

Thesis submitted in Partial Fulfillment of the
Requirements for the Degree of
Bachelor of Applied Sciences

In the School of Engineering Science
Faculty of Applied Sciences

Simon Fraser University
Fall 2023

APPROVAL

Name: Mehar Rehill

Degree: Bachelor of Applied Science Honours

Title of Thesis: Methods for the estimation of depth-resolved attenuation in OCT

Dr. Cheng Li, P.Eng.
Director, School of Engineering Science

Examining Committee:

Dr. Pierre Lane, P.Eng.
Associate Professor, School of Engineering Science

Dr. Mirza Faisal Beg, P.Eng.
Professor, School of Engineering Science

Adrian Tanskanen
BC Cancer Research Institute

Date Approved: December 11, 2023

Abstract

Cancer is one of the major causes of mortality, accounting for one in six deaths worldwide in 2020 [1]. The majority of cancers can be prevented , cured , or reversed if early detected. Early diagnosis and screening are vital components, with screening focusing on detecting cancer before the symptoms manifest, and diagnosis involving the identification of cancer in its early stages through methods like biopsies and imaging techniques [1].

Optical coherence tomography (OCT) has shown potential for early cancer diagnosis, due to its non-invasive nature and potential to guide biopsies site selection, reducing the invasiveness of certain procedures by enabling the clinicians to obtain fewer biopsies and minimizing errors associated with surgical biopsies [2] [3]. Researchers have proposed several models linking the attenuation coefficient (μ), which describes the exponential decay of the OCT signal, with tissue optical structural properties. Presently , two methods, layer-wise extraction through curve fitting and depth-resolved methods, are employed for attenuation coefficient calculation. However, challenges persist in achieving accurate and precise estimations.

This thesis entails a comparison of four methods to calculate the attenuation coefficient from OCT intensity data-: slope-fitting, Vermeer, Jain Lui and Kaiyan Li. Validation of theses methods on various types of milk serves as a preliminary evaluation, with further comparisons of estimated attenuation coefficients from OCT images against measurements from a power meter using various intralipid concentrations. The identified optimal algorithm is subsequently applied to OCT images for both cancerous and normal oral tissues.

The study extends its evaluation to explore critical factors influencing the performance of the four methods. Pre-processing, including frames averaging, is found to enhance data quality and signal-to-noise ratio (SNR). The noise floor, particularly prominent at greater imaging depth, poses challenges common to all methods. Overlooked confocal effects, especially in samples with lower attenuation coefficients, contribute to underestimation in the Jain Lui and Kaiyan Li methods. While the validation experiments establish a linear relationship between intralipid concentration and attenuation coefficient, multiple scattering at higher intralipid concentrations challenges the assumption of constant backscattering fraction. Each method exhibits strengths and shortcomings, emphasizing the need for further research to explicitly incorporate confocal effects and multiple scattering to enhance depth-resolved algorithms for improved biomedical applications.

Acknowledgments

I extend my gratitude to Dr. Pierre Lane for the invaluable opportunity to be part of the BC Cancer Research Center for the past 8 months. This period has been instrumental in my personal and professional growth, exposing me to diverse and engaging areas of biomedical engineering.

I express my profound appreciation to my technical supervisor, Adrian Tanskanen, for his unwavering support and guidance throughout the entire thesis process. His mentorship, both academically and technically, played a pivoted role in shaping the trajectory of this work, I am particularly grateful for his constant supervision at every step.

Special thanks are extended to the integrative oncology team for their contributions of reasoning and thoughtful insights during team meetings. I would also like to express my gratitude to them for providing the essential clinical oral images for this project.

Acknowledgment is also due to my family for their support in my endeavors. Their encouragement has been a source of strength and motivation. Lastly, I extend my thanks to all the faculty, staff, and my classmates in the SFU School of Engineering Science.

Table of Contents

List of Figures

List of Tables

List of Aberrations

DR	Depth-Resolved
FWHM	Full Width Half Maxima
H&E	Hematoxylin and Eosin
MIP	Mean Intensity Projection
NIR	Near Infrared
OCT	Optical Coherence Tomography
RPC	Rotatory Pullback Catheter
SNR	Signal-to-noise ratio

Chapter 1 Introduction

1.1 Problems and Motivation

The human body is a remarkable wonder, which may sometimes succumb to cancer, reminding us of its fragility and susceptibility, testing and challenging the limits of modern medical advancements. Cancer often a fatal disease, is caused due to the interaction of an individual's genetic factors and external carcinogenic agents, rendering it a heterogenous disease with unique prognoses and diagnoses for each patient [1]. In Canada, its is responsible for a staggering 28.2% of all deaths, making it a leading cause of mortality [4].

According to the American Cancer Society, detecting cancer early can decrease cancer mortality and greatly improve the chances of successful treatment [1]. Several statistical data on oral cancer shows that patients with stage I oral cancer diagnosis has a 5- year survival rate of 71% whereas those with stages II-IV has the remaining 37%, highlighting the significance of early detection [5] [6]. Early detection of cancer is divided into two components: early diagnosis and screening. Screening involves detection of cancer prior to the onset of symptoms whereas diagnosis entails identification of cancer in its early stage using procedures like biopsies, pathological examination and imaging techniques [1].

At present, invasive biopsies and pathological examination are employed as the gold standard in early detection of cancer. However, cancer can be difficult to detect via imaging methods due to a variety of factors, including the size and location of the tumor, the density of surrounding tissue, and the sensitivity and specificity of the imaging technique used [7]. These factors emphasize the necessity for ongoing research and advancement of imaging technologies to enhance the early detection and diagnosis of cancer.

Optical Coherence Tomography (OCT) holds promise as an emerging imaging technique for the early detection of cancer. Its non-invasive nature and its capacity to provide extensive structural and functional information make it compelling avenue for exploration. OCT has the potential to aid in performing biopsies, potentially reducing the invasiveness of certain procedures by enabling clinicians to obtain fewer biopsies, better identify the margins of occult lesions and minimize false negatives [2] [3]. OCT operates on a similar principle of backscattered signals as ultrasound but uses broadband and near- infrared light (NIR) instead of high-frequency sound used in ultrasound. Due to the difference in the properties of light and sound OCT has shallow penetration and higher resolution as compared to ultrasound [8].

The interaction of light follows a consistent pattern: as light penetrates deeper into the sample, the intensity of the signal diminishes exponentially. This characteristic relationship, characterized by the decay in the strength of the backscattered signal as a function of sample depth, is quantified by the attenuation coefficient [9]. The motivation for measuring attenuation arises from the limitations of qualitative OCT intensity images. While these images offer valuable information, they do not provide a quantitative assessment of tissue scattering properties. However, through the calculation of the attenuation coefficient, we can possibly evaluate the optical characteristics of the sample, enhancing the capabilities of OCT in cancer detection and tissue analysis.

Currently two methods are used to calculate the attenuation coefficient: (1) layer wise extraction and curve fitting; and (2) depth resolved methods [10]. For the layer wise curve fitting method, the attenuation coefficient is linearly proportional to rate of change of the log of intensity over a homogenous medium, which makes the model appropriate only for specimens with little variation in optical properties with depth [11]. The depth-resolved (DR) method is the most recent method of modeling based on an assumption that all light is completely attenuated within the recording depth range and a fixed fraction of backscattered light is reflected of the attenuated light [12]. DR method has been frequently employed in intravascular OCT [11], diagnosis and monitoring of glaucoma [12] and several more diagnostic applications, but unerring and precise estimation of the attenuation coefficient still remains an important challenge.

This thesis is dedicated to a comprehensive comparison of four distinct methods for calculating the attenuation coefficient from OCT intensity data. The effectiveness of each method is assessed through a series of experiments conducted on different types of milk. Furthermore, the calculations of attenuation coefficients obtained from OCT images of intralipid are compared with measurements derived from a power meter. Once we have identified the most suitable algorithm among the four, we proceed to apply it in generating attenuation coefficient images for both cancerous and normal appearing oral tissue.

1.2 Background

1.2.1 Optical Coherence Tomography

Optical Coherence Tomography is an optical technique, which provides DR images of tissue structures from backscattered light a higher resolution than ultrasound. [13] [14]. OCT works on the principle of low-coherence interferometry, signal from a low coherence source of light is divided into reference arm $E_r(t)$ and sample arm $E_s(t)$ pathways (Figure 1) [14]. The reference arm consists of a mirror at which the signal is reflected from a known distance meanwhile the light along the sample arm is backscattered after interaction with the specimen. The combination of these signals results in interference fringes (destructive and constructive) which are detected at the detector as shown in Figure 2 [9]. Based upon different types of OCT spectral interferograms (measured in wavenumber, k-space), they undergo various signal processing methods in both the time and Fourier domain to further convert them into A-scans and B-scans (measured along the physical optical axis, z-space) [14].

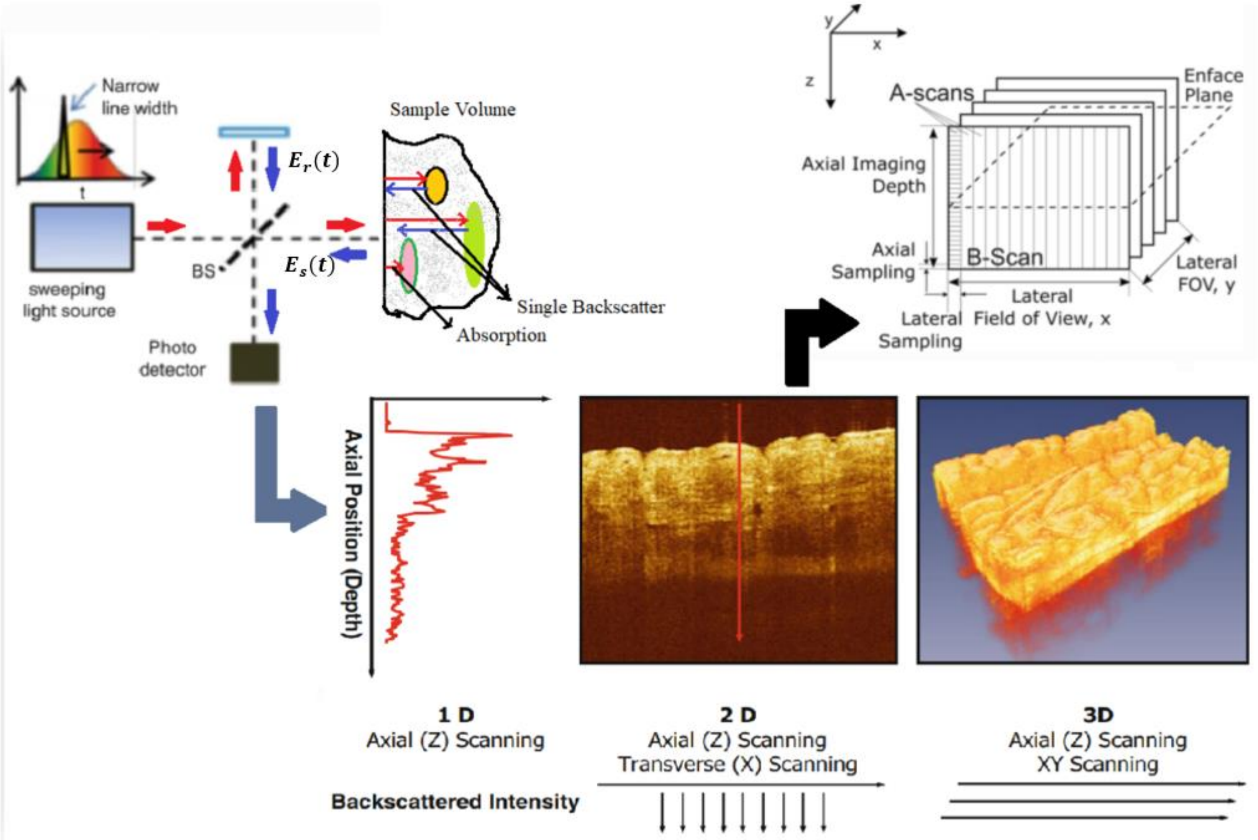

Figure 1 *Interaction of light with tissue and compartments and the acquisition of the image [14] [15].*

There are three common OCT technologies: Time-domain (TD-OCT), Spectral- domain (SD-OCT) and Swept-Source (SS-OCT) [16]. In TD-OCT the path difference in the reference arm is modulated to obtain the profile of the sample, which is observed as the interference pattern at the detector [15]. However, in SD-OCT a broad-band light sources is used and the point detector is replaced by spectrometer where spectral information (intensity as a function of wavelength) is used to generate A-scans instead of mechanical scanning of the optical path length [15] [17]. In SS-OCT a light source undergoes wavelength sweeping across a broad bandwidth, and the time-based output of the detector is changed into spectral interference [17]. Both SD-OCT and SS-OCT are categorized as Fourier domain techniques. This classification stems from their reliance on Fourier analysis to extract depth information from the collected spectral data.

The OCT image provide diverse tissue information from the specimen and can reveal underlying abnormalities without the requirement for invasive biopsies [18]. For example, as shown in Figure 2, we can observe the differences between normal and cancerous rectal tissue. In the OCT images, the mucosa and submucosa appear undefined and irregular, a characteristic that is further confirmed by the corresponding H&E images of the rectal tissue.

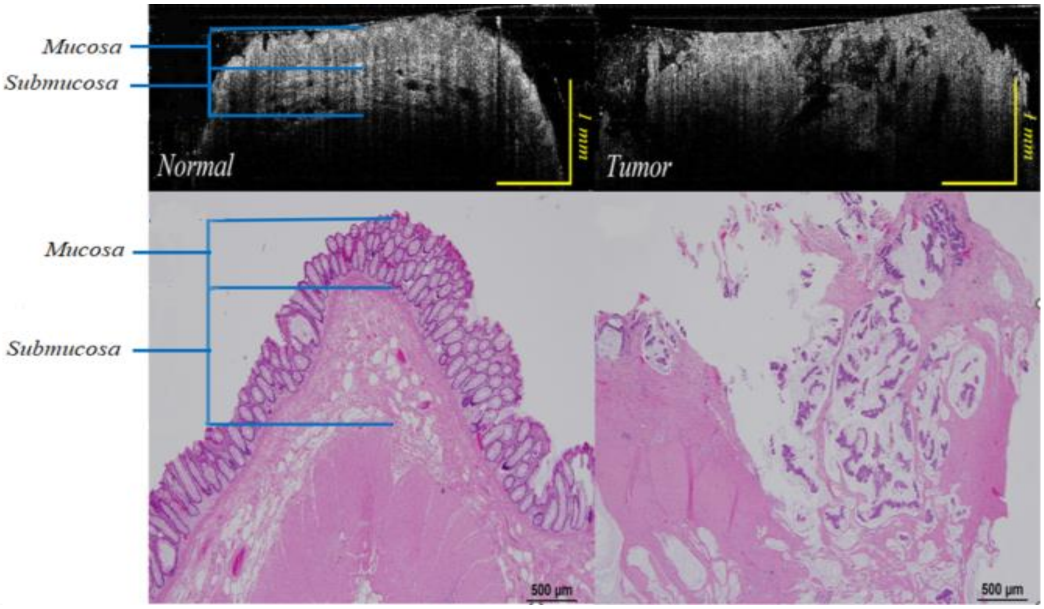

Figure 2 *Top left) OCT image of normal rectal tissue; Top Right) OCT image of rectal tumor; Bottom left) H&E image of the normal rectal tissue; Bottom right) H&E image of rectal tumor. (The site of the tissue is not specified) [19].*

1.2.2 OCT system parameters

When discussing an OCT system, the essential parameters to consider are axial resolution, lateral resolution, and imaging depth (along with the related confocal effect). The axial and lateral resolution of an OCT system are decoupled. Axial resolution is defined as the ability to distinguish between two points in the axial direction of the imagining beam [20], it is determined by the coherence properties of the light source (spectral FWHM) and the sampling of the signal at the detector. Axial resolution is given by [15],

$$\Delta z = \frac{2\ln(2)\cdot\lambda^2}{\pi\Delta\lambda} \qquad \text{Eq (1)}$$

where $\Delta\lambda$ is the bandwidth of light source. To achieve a good axial resolution, it is necessary to increase the bandwidth while simultaneously decreasing the wavelength [21].

The lateral resolution in an optical system pertains to its ability to distinguish between two points situated perpendicular to the axial direction of the beam. This crucial parameter is influenced by the system's numerical aperture (NA), which essentially characterizes the angle at which light is focused. NA is determined by the focal length and diameter of the lens. The lateral resolution is contingent on several factors, including the choice of lens, the materials aiding in the focusing process (NA), the wavelength of light, and the sampling density, as defined by Eq (2) [18] [24].

$$\Delta x = \frac{0.61\lambda}{NA} \qquad \text{Eq (2)}$$

When it comes to optimizing the lateral resolution, one can consider adjusting the numerical aperture of the system. Increasing the NA can enhance lateral resolution, but this must be balanced against the potential compromise it poses to the system's depth of focus, often referred to as the confocal factor.

Achieving good imaging depth in tissue samples with OCT requires the use of a coherent light source with minimal absorption by the sample, which is why OCT typically operates at wavelengths around 1300nm (NIR). As lower wavelengths are absorbed more by water, which is abundant in tissue it limits the penetration depth in OCT. However, longer wavelengths have lower scattering which on the contrary improves the imaging depth of the sample [9].

The confocal effect plays a critical role in optical systems by significantly impacting imaging depth. It allows optical systems to capture high-resolution images at specific depths within a sample while effectively rejecting signals originating from other depths further resulting in high signal-to-noise ratio (SNR) [12] [15]. However, towards the edges of the imaging depth, the beam width increases but backscattered light will still be captured from these points. The intensity of this light will be decreased compared to the backscattered signal closer to the optics true focus. When dealing with materials characterized by higher attenuation coefficients, there is a notable phenomenon: these materials tend to scatter incoming light more rapidly as it penetrates the substance. As a consequence, the imaging depth is notably reduced, and the optical signals detected from deeper layers of the sample tend to weaken. This reduction in signal strength makes it considerably more challenging to visualize structures or anomalies that exist beyond a certain depth within the sample. In summary, the confocal effect's interaction with materials possessing higher attenuation coefficients can significantly limit the depth at which imaging is feasible, subsequently affecting the quality and clarity of the obtained optical images.

1.2.3 Attenuation Coefficient

The power of a coherent light source travelling through a medium is attenuated along its path, as the light interacts with the substance of varying refractive index causing absorption and scattering [9]. The attenuation coefficient describes the rate at which the intensity of light decays into the tissue. The power per unit area (irradiance) of a coherent light beam propagating though a homogenous medium at position z, is given by Lambert-Beer’s law [12],

$$\boldsymbol{L(z) = L_0 e^{-\mu z}} \qquad \text{Eq (3)}$$

Where L(z) is the irradiance of the beam after propagating through the homogenous medium over a distance z (mm), L_0 is the irradiance of the incident light in Watt/meter^2 and μ is the attenuation coefficient (mm^{-1}). The larger the attenuation coefficient, the faster the exponential decay of the light and vice versa [14]. The attenuation coefficient depends upon attenuation of light due to absorption μ_a (mm^{-1}) and attenuation of light due to scattering μ_s (mm^{-1}) [13],

$$\mu = \boldsymbol{\mu_a} + \boldsymbol{\mu_s} \qquad \text{Eq (4)}$$

The calculation of attenuation coefficient is primarily influenced by scattering due to the minimal absorption at NIR wavelength. Analyzing the backscattered signal in OCT allows for the calculation of the attenuation coefficient [9]. Various models like exponential curve fitting method and depth resolved method, relating attenuation coefficient and tissue optical structural properties has been proposed.

1.3 Thesis Structure

Chapter 2 reviews the methods to estimate attenuation coefficient from the literature that will be employed in this work. Beginning with the traditional slope fitting method, this chapter navigates through an exploration of depth-resolved methods. It encompasses renowned methodologies such as Vermeer, Taylor, Jain Lui and Kaiyan Li, with each approach being presented in terms of its mathematical principles, advantages and limitations.

Chapter 3 describes the methodology employed in the thesis. It provides a comprehensive account of the practical implementation of various techniques, which include slope fitting, and the methods of Vermeer, Jian Lui and Kiayan Li using five distinct milk samples. Furthermore, this chapter outlines the design and execution of validation experiments, which involve the variation of intralipid concentrations. Lastly, it offers guidance on the application of most effective algorithm for handling *in vivo* images.

Chapter 4 offers a straightforward and concise presentation of the objective outcomes derived from the experiments detailed in the preceding methods section.

Chapter 5 presents a discussion and analysis of the results. Here, we delve into detailed explanations and justifications for the findings of our experiment.

Chapter 6 explores potential areas for future research in the field of attenuation coefficient and provide a summary of the main findings and insights.

Chapter 2 Previous and Related Works

2.1 Exponential curve fit method

One of the long-established methods to determine attenuation coefficient is from OCT data is by fitting an exponential curve through OCT depth profiles. The Beer-Lambert law (Eq (5**)**) underlies the fundamental principles of OCT signal formation and interpretation. It helps to explain how the attenuation of light as it passes through tissue provides information about tissue properties including absorption and scattering. In the context of OCT, the power of the signal detected at the detector is proportional to the reflected intensity which is scattered at a certain depth in the homogenous medium, it is formulated as [12],

$$\boldsymbol{I(z) \propto e^{-2\mu z}} \qquad \text{Eq (5)}$$

where $I(z)$ is the reflected intensity at the detector and 2z in the exponent is due to the propagation of the light through the medium twice. As we see in Eq (5**)** the signal strength decreases exponentially as the light travels deeper into the sample and the relationship between the backscattered irradiance and the depth of the sample is described by the attenuation coefficient. The attenuation coefficient is further estimated by differentiating the logarithm of the reflected signal [12].

In Figure 3A and Figure 4A, I have stimulated the irradiance of the OCT signal using Eq (6) at different depths and with different attenuation coefficients to display the exponential relationship of the backscattered irradiance and the depth of sample. The graphs in Figure 3 and Figure 4 are produced by the steps outlined in Vermeer (Section 2.2.1) using Eq (6) [12].

Plotting the logarithm of the irradiance helps to make the signal more visible by compressing the dynamic range of the data [22]. Since the logarithm of an exponential function is a linear function plotting the logarithm of the signals results in a linear display of the data [23], henceforth making it easier to see the variations in the signal intensity at different depths in the sample.

Figure 3B and Figure 4B illustrates a stimulated homogenous phantom using Eq (5**)**, with the front surface moved back in the steps of 400 µm (imaging depth). Figure 4A and Figure 4B illustrates stimulated homogenous phantom with different attenuation coefficients µ=10 mm^{-1}, 5 mm^{-1}, 2 mm^{-1} and 1 mm^{-1} implementing Eq (6) at the same imaging depth, although to see the different exponential decay rate of the OCT signal with different attenuation coefficient on a linear scale they are plotted at different imaging depth.

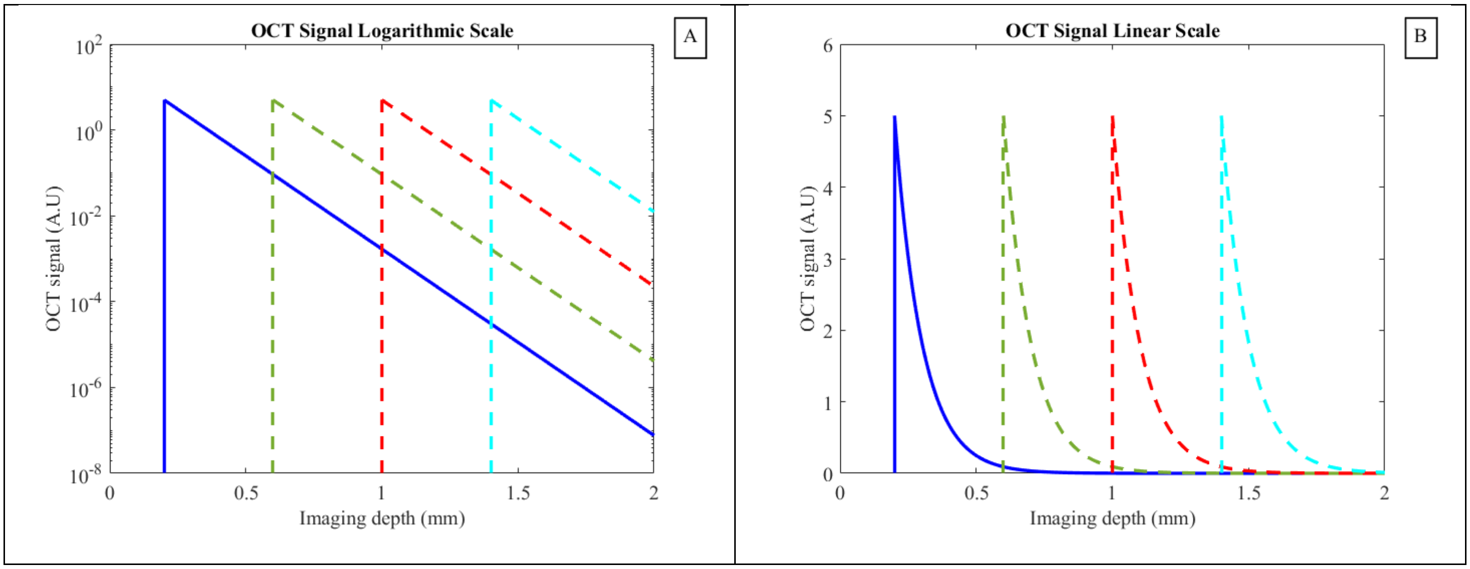

Figure 3 *(A) represents stimulated OCT signal at different imaging depth on a logarithmic scale (B) represents stimulated OCT signal at different imaging depths on a linear scale.*

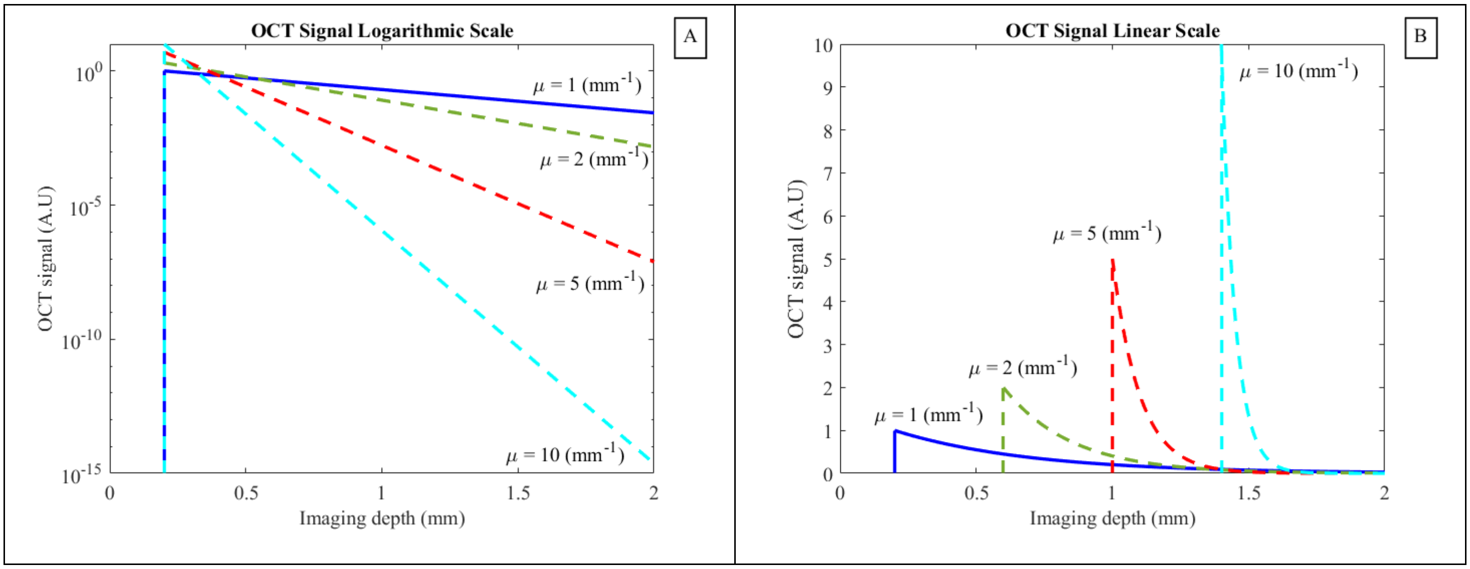

Figure 4 *(A) represents stimulated OCT signal at different attenuation coefficient on a logarithmic scale (B) represents stimulated OCT signal at different attenuation coefficient and imaging depths on a linear scale.*

Analyzing the logarithmically scaled OCT intensity in Figure 3A and Figure 4A, the variation in slopes resulting from different attenuation coefficient values is apparent. More realistically, OCT signals are subject to phenomena such as speckle noise and variable image quality making these curves fits challenging. It becomes even more challenging when dealing with heterogeneous samples like oral tissue, leading to poor estimations of attenuation coefficient [11].

Fitting each A-line for an entire volume can also be quite demanding computationally and time-wise. In addition, since the fitting method assumes that the attenuation coefficient is constant over a segment, even a small change in the attenuation can cause a loss of detail and resolution.

2.2 Depth- Resolved methods

This section offers a concise overview of various methods in the literature for estimating depth-resolved attenuation coefficients. Each method from the early Vermeer approach to more recent developments like the Smith, Lui, and Li methods are briefly described, highlighting their individual contributions and areas of focus. Additionally, the section acknowledges the limitation of uniform assumptions regarding light scattering in heterogeneous tissues, paving the way for variable backscattering models. These brief descriptions provide valuable insights into the evolution of depth-resolved techniques for accurately estimating attenuation coefficients over the years. Figure 5 at the end of the chapter summarizes previous works and related describing the development for estimation of attenuation coefficients over the years until the present.

I have carefully selected the Vermeer, Jain Lui and Kaiyan Li methods as our primary approaches for estimating depth-resolved attenuation coefficients. These methods have been chosen for their distinct attributes and capabilities in providing insights into tissue properties. I will delve into comprehensive exploration of each method in the upcoming method section, where I will elucidate the details of their implementation.

2.2.1 K.A. Vermeer model 2013 – Vermeer method

The approach of curve fitting an A-line has a downside, it only provides and average measurement of attenuation and misses the varying information with depth. In 2013 Vermeer et al, proposed a method which allows for depth resolved measurement of the attenuation coefficient in an OCT signal. This method is built on an assumption that all light is attenuated within the recorded imaging depth and the back scattered light that is reflected is a fixed fraction of the attenuated light. According to the Vermeer method, the backscattered irradiance $I(z)$ detected at the detector in Wm^{-2} is given by [12],

$$\boldsymbol{I(z) = \alpha\beta\mu(z)L_0 e^{-2\int_0^z \mu(u)du}} \qquad \text{Eq (6)}$$

Where α is the fixed fraction of absorbed light that is reflected, β is the detector's quantum efficiency, which tells us how the light's intensity per depth is turned into a digital signal. $\mu(z)$ is the attenuation coefficient (mm^{-1}) at depth z (mm), L_0 is the incident irradiance (Wm^{-2}) at depth z=0. To estimate the attenuation coefficient over the depth z, Vermeer integrates Eq (6) with the boundary condition of $I(\infty) = 0$ over a limited depth range D (mm^{-1}) of the OCT system, to yield [12],

$$\boldsymbol{\mu}(\boldsymbol{z}) = \frac{\boldsymbol{I}(\boldsymbol{z})}{\mathbf{2}\int_{\boldsymbol{z}}^{\boldsymbol{D}} \boldsymbol{I}(\boldsymbol{u})\boldsymbol{du}} \qquad \text{Eq (7)}$$

Eq (7) describes the attenuation coefficient in a continuous domain. To make it suitable for practical use, we need to discretize it. The OCT signal $I(z)$ is integrated over small distance and pixel size Δ and the final equation after integration [12],

$$\boldsymbol{\mu}[\boldsymbol{i}] \approx \frac{\boldsymbol{I}[\boldsymbol{i}]}{\mathbf{2}\Delta\sum_{\boldsymbol{i}+\mathbf{1}}^{\infty} \boldsymbol{I}[\boldsymbol{i}]} \qquad \text{Eq (8)}$$

Since the backscattered signal relies on the local attenuation coefficient, there is no reliance on a complex manual segmentation process. The Vermeer method does not require constant attenuation coefficient within any specific segment. It has proven to offer better axial resolution and provides attenuation coefficients for each individual pixel without the need to predefine layers, which makes it a good fit for studying heterogenous specimens.

2.2.2 T. Smith model 2015 – Smith method

The Vermeer method has few shortcomings. It does not take into account the confocal factor and the sensitivity roll-off [24]. With the Vermeer method, the focal plane was set above the sample, which not only lowered the SNR but also limited its usefulness in clinical settings [24].

In 2015, G.T.Smith proposed a method which considered the confocal factor and more comprehensive model for the axial point spread function to estimate attenuation coefficient. It also used a new noise reduction technique to clean up their data which is a bit of a trade off as its is computationally expensive [24]. The Smith method works really well for samples with horizontal layers, but it does not perform well with tissues that have different shapes and features [24].

2.2.3 Jain Lui model 2019 – Lui method

In the Vermeer method, there is a challenge when it comes to estimating the attenuation coefficient, especially towards the end of the depth profile. Since OCT has limited depth range limited by its sensitivity (noise floor), it tends to overestimate the scattering coefficient at depths near the maximum (N-1). The Vermeer method assumes that beyond a certain depth (z), the OCT signal is fully absorbed and any depths further (ranging from z+1 to the maximum depth, N) contain only noise, this assumption is suitable for scenarios with shallow imaging depths. However, as the imaging depth increases, this assumption becomes less accurate. As we approach the noise floor, the signal intensity tends to diverge towards infinity, resulting in a loss of valuable information [25].

In 2019, Jain Lui introduced a novel method to improve the depth related accuracy of the attenuation coefficient $\mu[z]$ while considering the deviations which occur when the signal intensity approaches the noise floor [25],

$$\boldsymbol{\mu[z]} = \frac{\boldsymbol{I[z]}}{\boldsymbol{2\Delta \sum_{i=z+1}^{\infty} I[i] + \frac{I[N]}{\mu[N]}}} \qquad \text{Eq (9)}$$

Lui’s method involves a mathematical formula (Eq (9)) that considers various factors. It considers the backscattered irradiance at different depth $I[z]$ and the unknown attenuation coefficient at the last point ($\mu[N]$), which is determined through fitting an exponential curve [25].

2.2.4 Kaiyan Li model 2020 – Li method

Jain Lui’s method replaces the background noise in the data with a calculated pattern that makes the Vermeer method’s assumption about complete attenuation in the given depth more accurate. However, the Lui method depends a lot on how precisely you fit the boundary value $\mu[N]$. In practice, this can create noticeable and randomly scattered bright or dark patterns in the final image that shows attenuation coefficient [26].

In 2020, Kaiyan Li introduced a method for calculating attenuation coefficient. The existing methods had some inaccuracies, either suggesting too much light was being absorbed at the surface or too little in deeper areas. The Li method corrected this by removing unwanted noise from calculations for the shallow areas and including an imaginary extension for deeper parts. These adjustments improved the accuracy of estimating attenuation coefficient [26],

$$\boldsymbol{\mu[n]} = \frac{\boldsymbol{A^2[n]}}{\boldsymbol{2\delta.\sum_{n+1}^{N} A^2[m]}}\left(\boldsymbol{1 - e^{-2\delta.\sum_{n+1}^{N}\mu[m]}}\right) \qquad \text{Eq (10)}$$

where $\mu[n]$ is the attenuation coefficient over a pixel n, $A[n]$ is the real-valued magnitude of a complex OCT A-line profile over n pixel, δ is the axial pixel and the coherence length of the low coherence beam, N is the number of pixels within each A-line, and $\mu[m]$ is the attenuation coefficient. Eq (10) is evaluated recursively, starting from n=N where the slope of the A-line tail was estimated using a fit, and progressing up to the tissue surface [26].

2.2.5 Variable backscattering fraction (α) models

Methods based upon the work by Vermeer et al assumes no variations in backscattering fraction (α) throughout the depth of the sample. In reality changes in tissue morphology (cell nuclear size, density and refractive index) cause variations in the angles and intensity light is backscattered. Methods like Cannon model (2021), Yaning PSF model (2021) and Yaning model (2023) keep the details of how the light is absorbed at various depths the same but do not rely on assumptions that light scatters uniformly [27]. Instead, they look at specific layers and estimate the attenuation coefficient separately [28].

Depth resolved methods struggled to distinguish if changes in tissue behaviour were due to tiny internal structures (like nuclei) or the size and concentration of these structures. Methods involving variable backscattering models helped reduce this ambiguity. Changes in light absorption in an area may indicate whether more particles are present or if there is an abnormality [11].

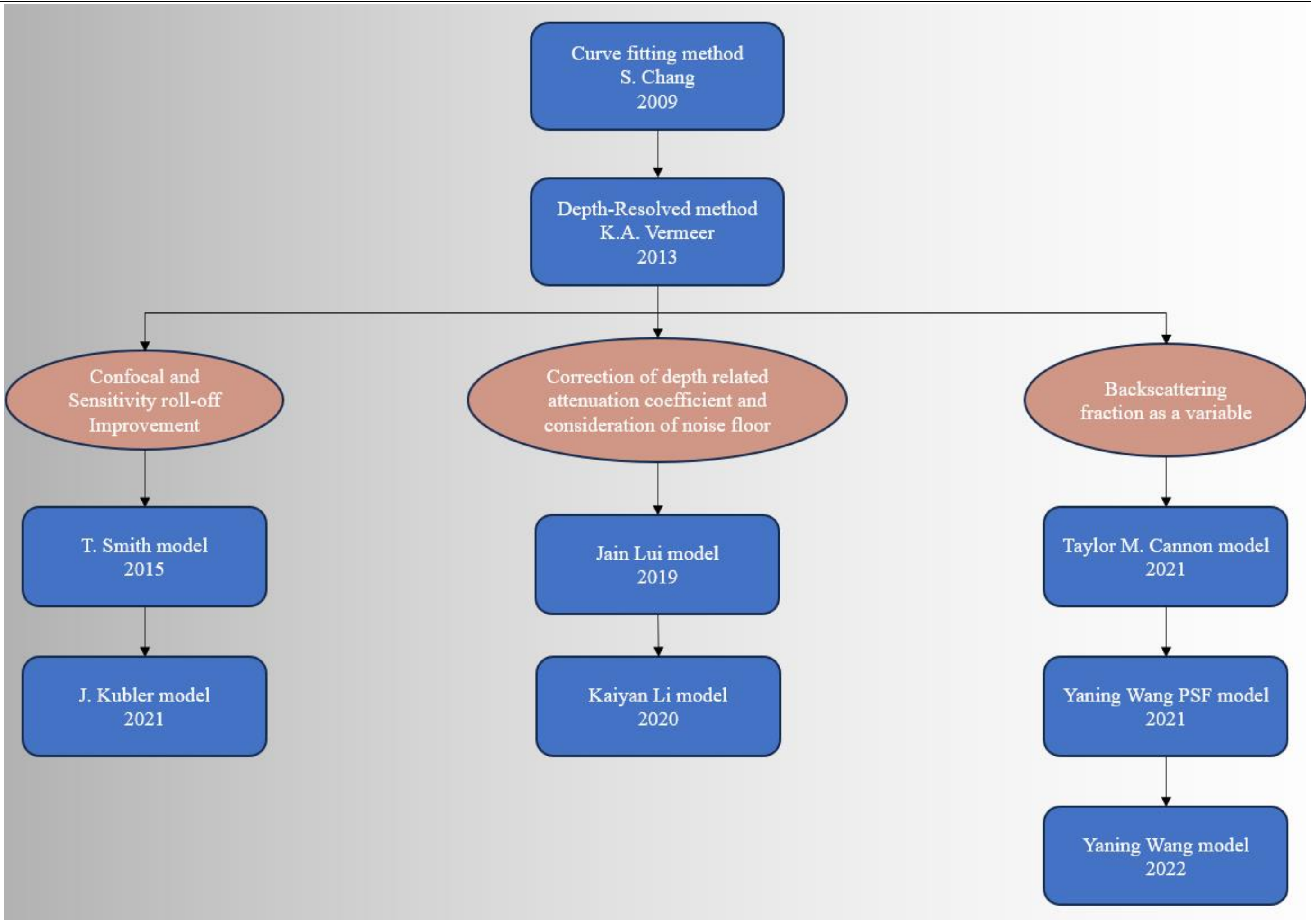

Figure 5 *Previous related work for the estimation of attenuation coefficient over the years.*

Chapter 3 Methods

3.1 OCT Dataset

The OCT dataset used to develop the algorithms was collected with wide-field OCT system at the BC Cancer Institute [29]. Figure 6 orients the reader to the coordinate system of the images captured by the system, which employs a rotatory pullback catheter (RPC). This probe has a dual motion—it rotates in an angular direction (θ) and is simultaneously pulled back in the (y) direction. Figure 6A demonstrates the 3D cylindrical coordinates of RPC. Here (z) signifies the imaging depth and the direction of the laser into the tissue, theta (θ) designates the catheter's rotation direction and speed and (y) indicates the pullback direction of the probe.

To simplify the complexity of the 3D imaging system I unwrap the cylindrical coordinate system to cartesian coordinate system represented in Figure 6(B-D). There are three types of OCT images based upon the unwrapped 2D coordinate system. Cross-sectional images (Figure 6B) are defined by θ and z axes; Longitudinal images (Figure 6C) are defined by the y and z axes; *en face* images (Figure 6D) are defined by θ and y axes.

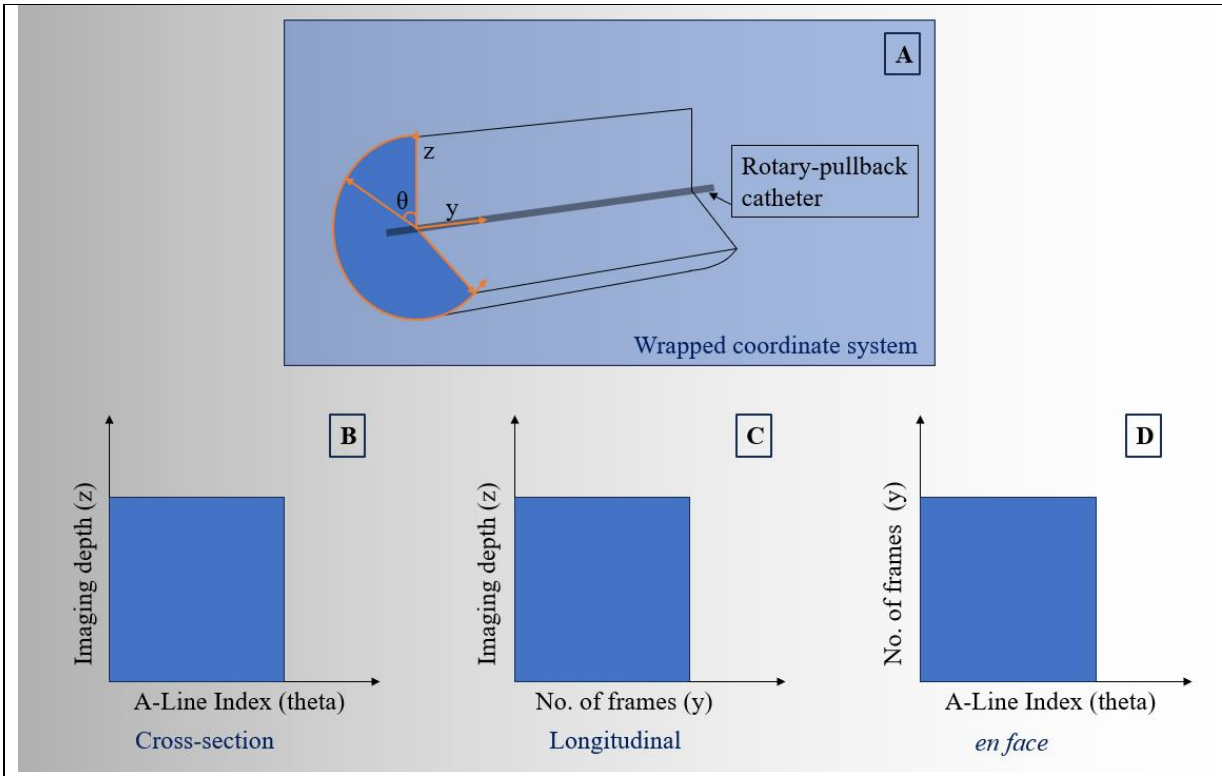

Figure 6 *(A)Rotatory pullback catheter unwrapped 3D coordinate system. (B) Cross-section coordinate system. (C) Longitudinal coordinate system.(D) en face coordinate system.*

The primary interest is in understanding variations in tissue structure in the z-direction, so I focus mainly on the cross-sectional images. Although longitudinal images provide information along the z-direction, and they are very large volume of data and delay in data acquisition means they do not offer real-time insights like cross-sectional images.

In this study, I used MATLAB R2022a for processing the data. To test the algorithms, I divided our work into two parts: (1) testing the algorithms on uniform phantoms and (2) validating the results. During the implementation phase, I worked with five different milk samples including almond milk, Earth’s own oat , Oatley oat barista, Silk coconut milk and 20% intralipid solution made from soya bean. All of the five milk samples at their delivered concentration were put in large test tubes and a probe was submerged in the centre of the test tube while 2 cm scan was taken. To validate the algorithms, I conducted an experiment with eleven samples containing varying concentrations of intralipid ranging from 0% to 20 % with an increment of 2%.

3.2 Algorithm Implementation

A major goal of this study was to contrast the selected methods for calculating the depth resolved attenuation coefficients from OCT images. Four methods to calculate the attenuation coefficient in milk samples were implemented. Algorithm implementation for the Vermeer, Jain Lui and Kaiyan Li methods consisted of four core stages as demonstrated in Figure 7: data loading, pre-processing, calculation of attenuation. For uniform samples the mean attenuation coefficient calculated from each approach were compared. This comprehensive approach enabled the evaluation and contrasting of the performance of these methods effectively, shedding light on their practical utility.

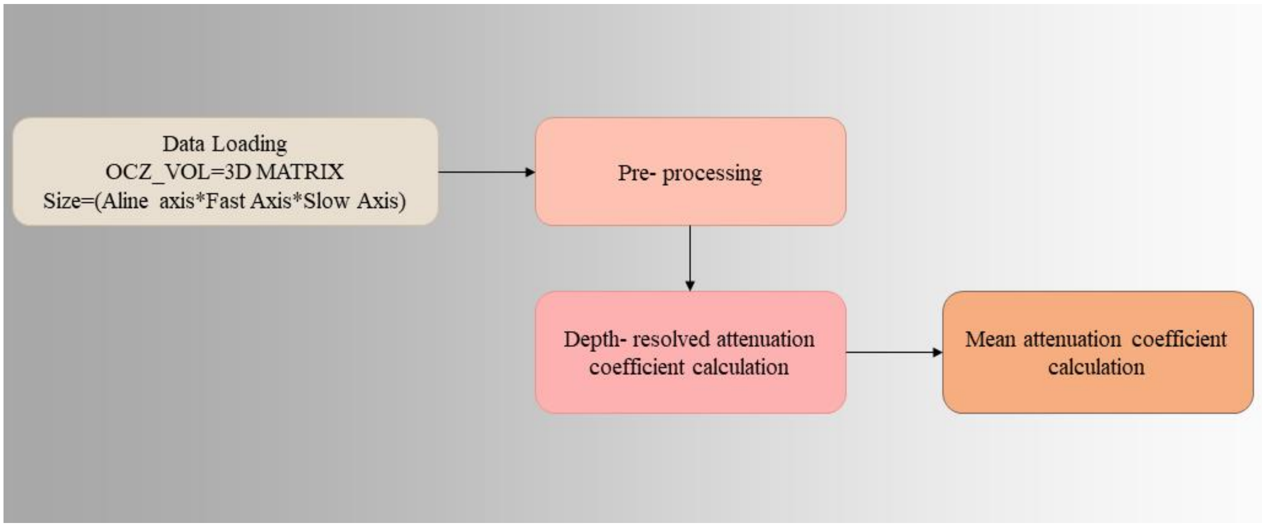

Figure 7 *Generalized flow chart for all of the four algorithms.*

3.2.1 Slope fitting method

To serve as a benchmark, the average attenuation coefficient was calculated by fitting the slope of the natural logarithm of each A-line (Section 2.1). The process begins by loading the data for each sample, followed by the essential step of data pre-processing.

During this pre-processing phase, I start by averaging the three cross-sectional images to enhance data quality and reduce noise, Figure 8A. Next, I carry out background subtraction, which involves setting a threshold to include only the tissue area for attenuation coefficient calculations. To achieve this, I calculate the median of every column over the entire cross-sectional image matrix and subtract if from the original frame, effectively eliminating any unwanted background elements (Figure 8B). Subsequently, we employ the 2-D median filter in MATLAB to mitigate speckle noise (Figure 8B). Following the pre-processing phase, I ask the user to specify the area of interest within a cross-sectional image (Figure 9), laying the groundwork for the subsequent calculations.

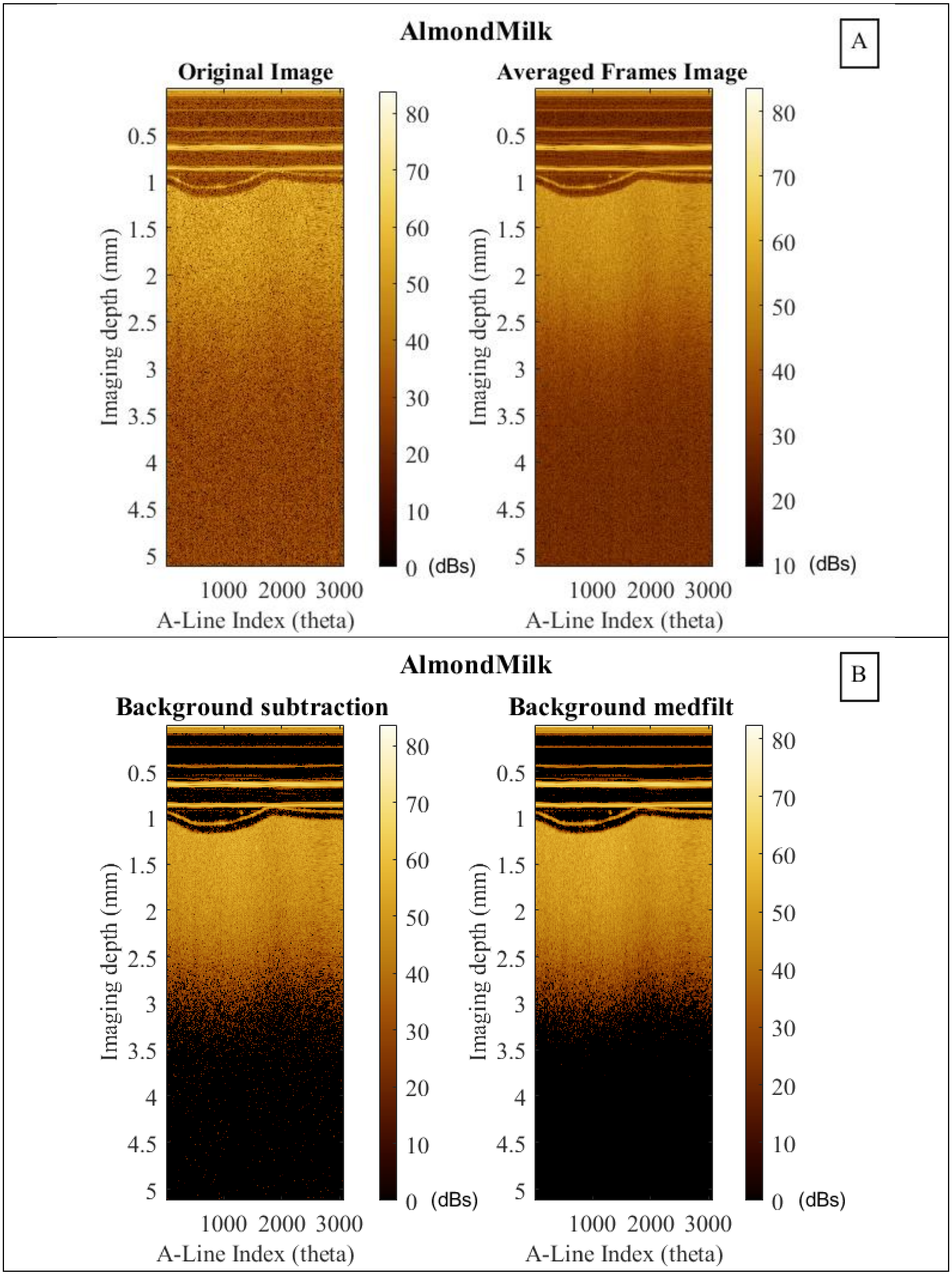

Figure 8 *(A) Original and Averaged Images of a cross sectional frame of almond milk. (B) Background subtracted and median filter images of a cross sectional frame of almond milk. Units for the color bar are in dbs.*

]

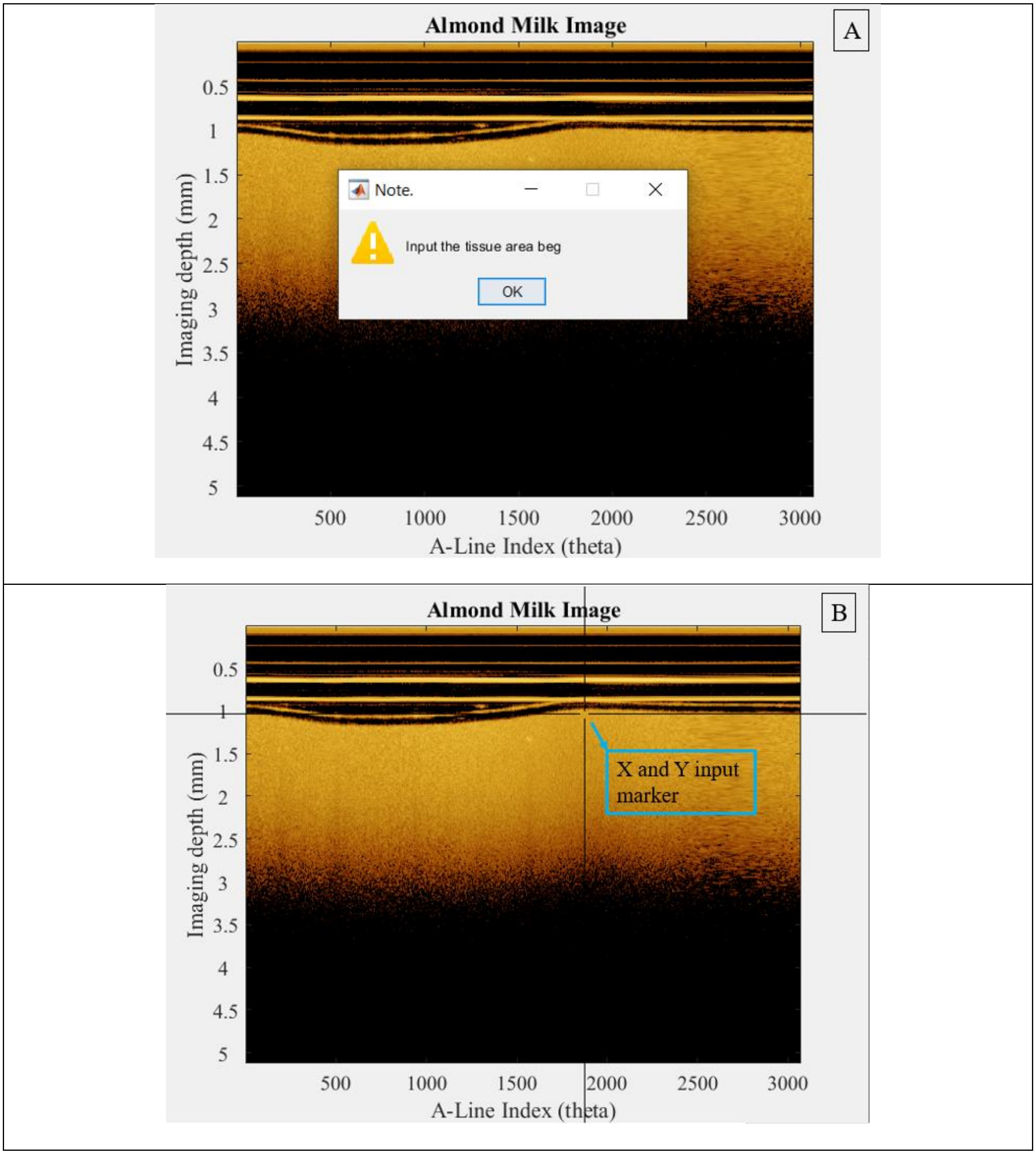

Note.

Input the tissue area beg

Figure 9 *(A) Almond milk showing input tissue beg window. (B) Highlighting the input marker for the inputting of the tissue beginning of an almond milk image.*

In Figure 10, we observe that the slope of the linear fit directly corresponds to the attenuation coefficient, μ(z), at the specific depth indicated. This observation forms the foundation for Eq (11). I initiate the process of conducting linear fits for each A-line, determining the slopes for every frame. The procedure commences with the utilization of an intensity-scaled A-line. Subsequently, I apply the natural logarithm to the A-line and execute a linear fit over a specific interval defined by the area of interest. The resulting best-fit slope, denoted as μ in Figure 10, is then multiplied by (-1/2) in Eq (11).

Finally, I compute the average of slopes for all A-lines across the cross-sections throughout the entire volume. This calculation results in the determination of the mean attenuation coefficient for each sample.

$$\boldsymbol{\mu(z) = -\frac{1}{2}\frac{\Delta \ln (I(z))}{\Delta z}} \qquad \text{Eq (11)}$$

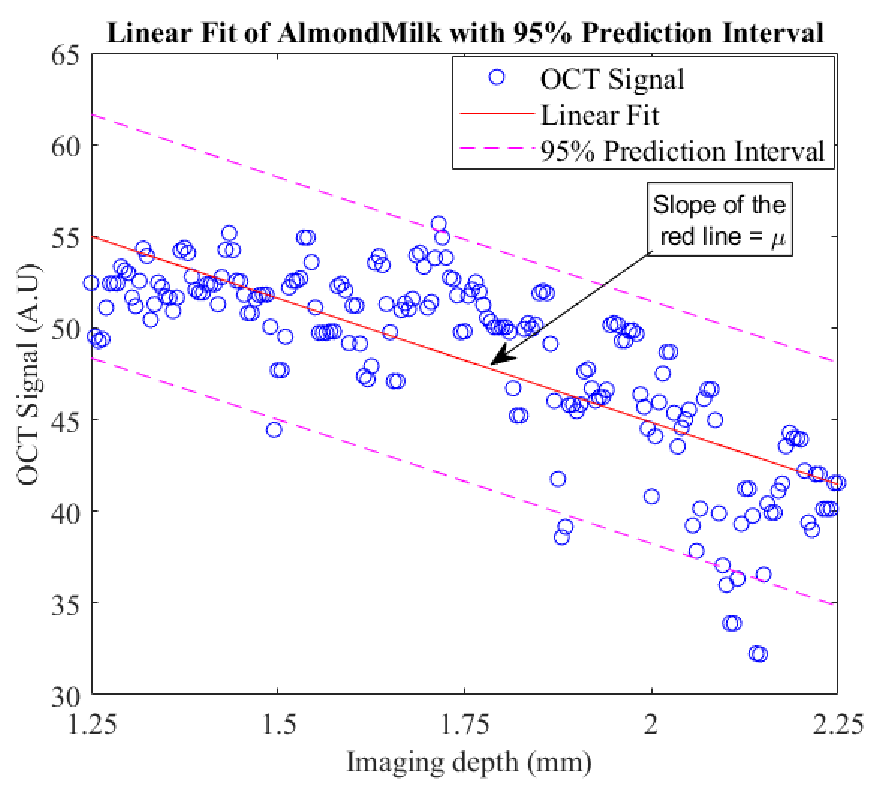

Figure 10 *Showing linear fit of a sectioned A-line of a frame of almond milk.*

3.2.2 Vermeer Method

In the Vermeer method, the initial stages of data loading and pre-processing mirror those of the slope fitting method. However, with the Vermeer approach, I go further by calculating the attenuation coefficient using Eq (8). Figure 11 show the OCT cross-sectional image and depth-resolved attenuation coefficient of almond milk. To assess the method's performance, I compute the mean attenuation coefficient within the specific user-defined region of interest for all the samples.

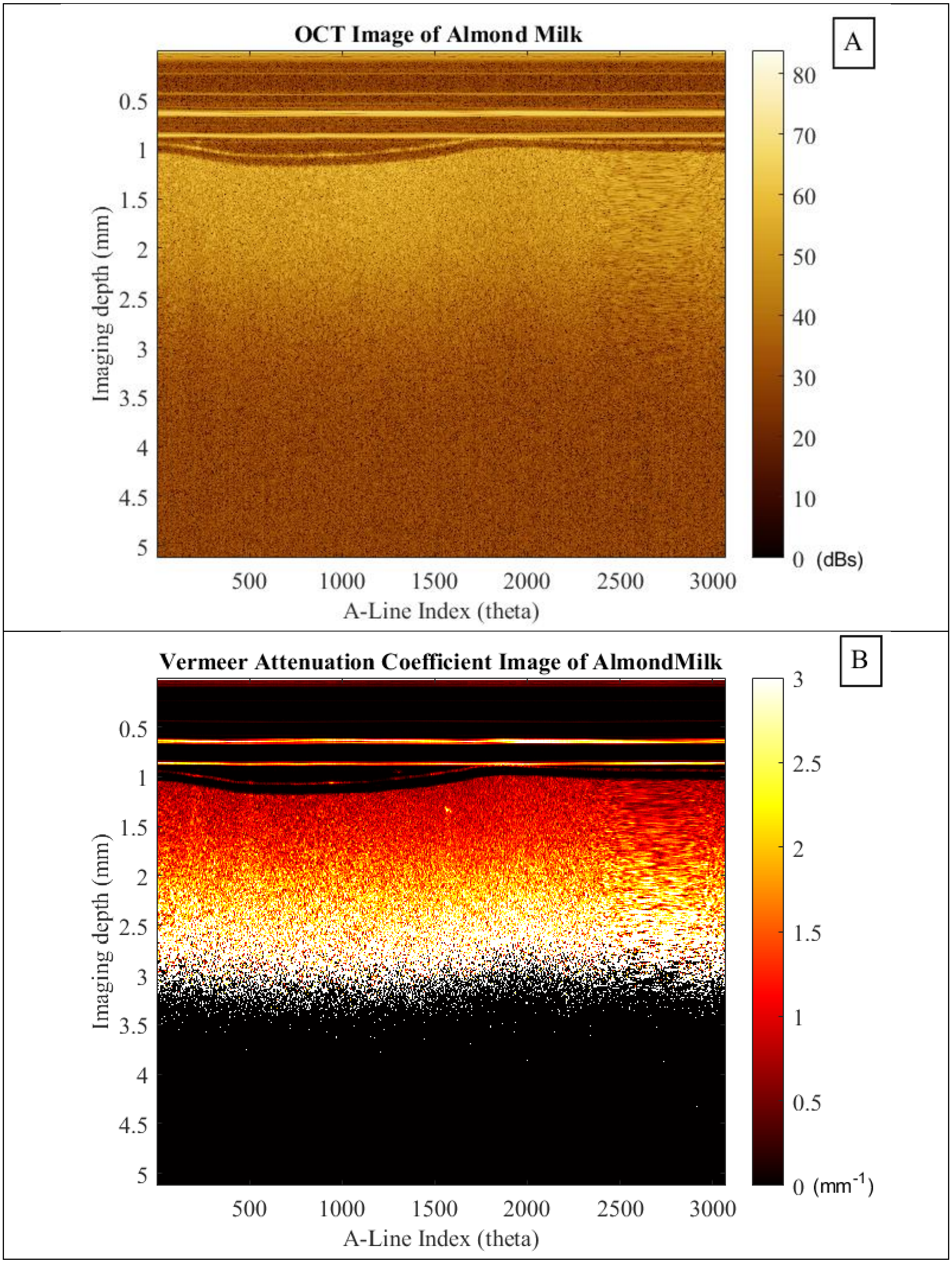

Figure 11 *(A) OCT image of a cross- sectional frame of almond milk. (B)Vermeer attenuation coefficient image of a cross- sectional frame of almond milk.*

3.2.3 Jain Lui Method

In the Jain Lui method, the process initiates with data loading and frame averaging, similar to the Vermeer method. However, the pre-processing approach in Jain Lui differs slightly. I start by removing the noise floor from the frames through a two-step process. First, I ask the user to input the noise floor using the same point input (Figure 9) in a cross-sectional image. Subsequently I take the mean of the intensity values of the inputted noise floor area. I smooth the signal using a 2D Gaussian blur of a 7.5 kernel size. Second, I create a binary mask which sets the values 6dB above the noise floor to one, as shown in Figure 12. With the mask in place, I find the location of the end of the tissue and proceed to calculate the fitting length for determining μ[N] in Eq (9).

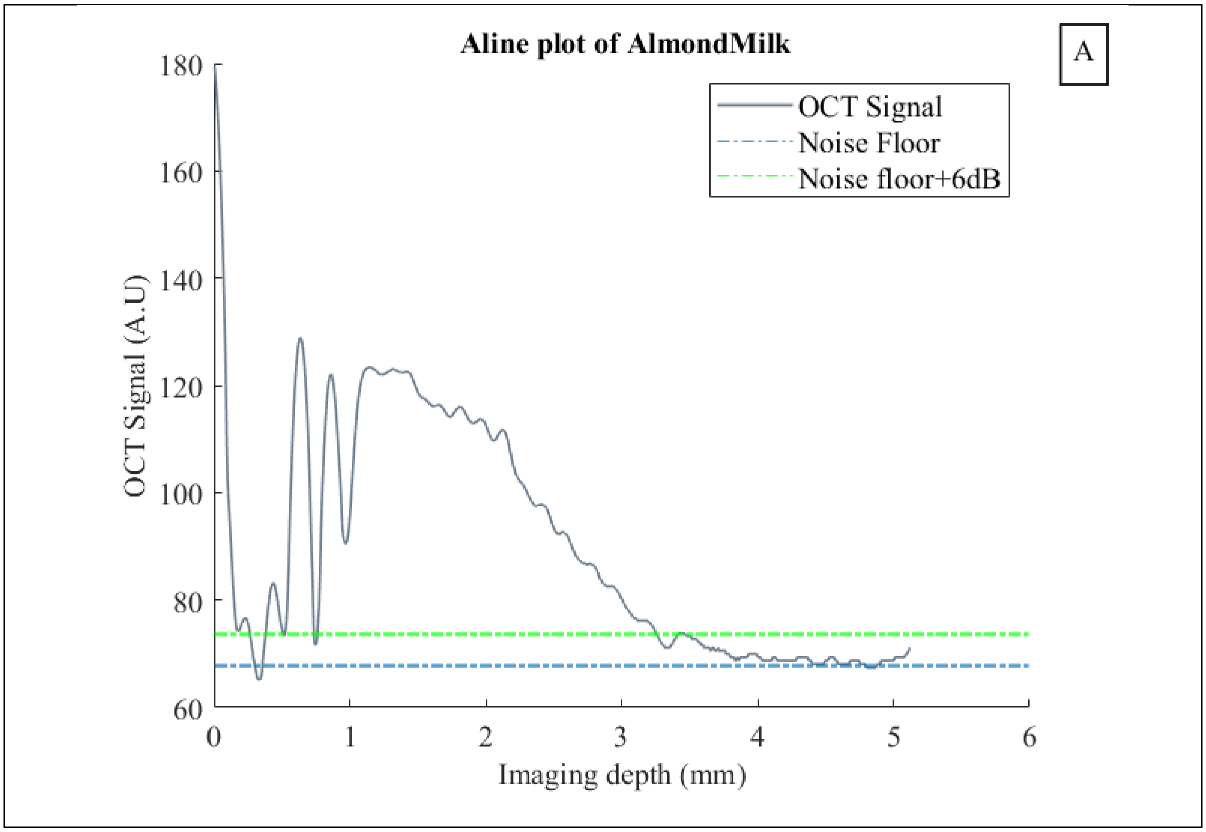

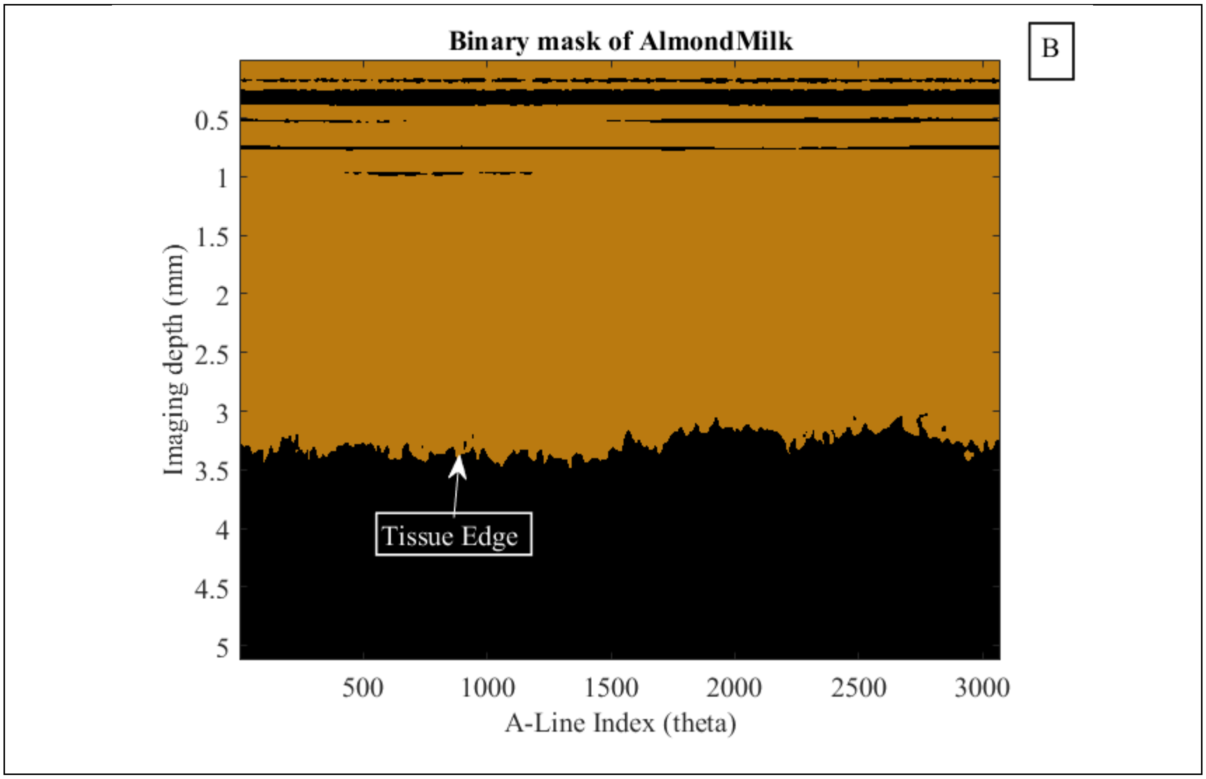

Figure 12 *(A) A-line plot of almond milk. (B)Binary mask of a cross- sectional frame showing sample edge of almond milk.*

To establish the fitting length, I conduct linear fitting on the last 20 pixels of the A-line truncated at 6dB. If the resulting correlation coefficient (R) falls below 0.95, the fitting interval is incrementally increased by 20 pixels until R reaches 0.95 or reaches the maximum limit of 200 pixels from the tissue end. This constraint is implemented to prevent deviation too far from the tissue end, as illustrated in Figure 13A.

It's important to note that the Lui paper employed an exponential fit ($y = e^{-2\mu z} + b$) instead of a linear fit to determine μ[N] Eq (9). Additionally, they used the standard deviation of the fit, not the correlation coefficient, to determine the length [25]. This represents a deviation from the method published by Jain Lui. Once the fitting length is determined, the value μ[N] is obtained for each A-line. Subsequently, the Jain Lui attenuation coefficient is calculated using Eq (9), as depicted in Figure 13B.

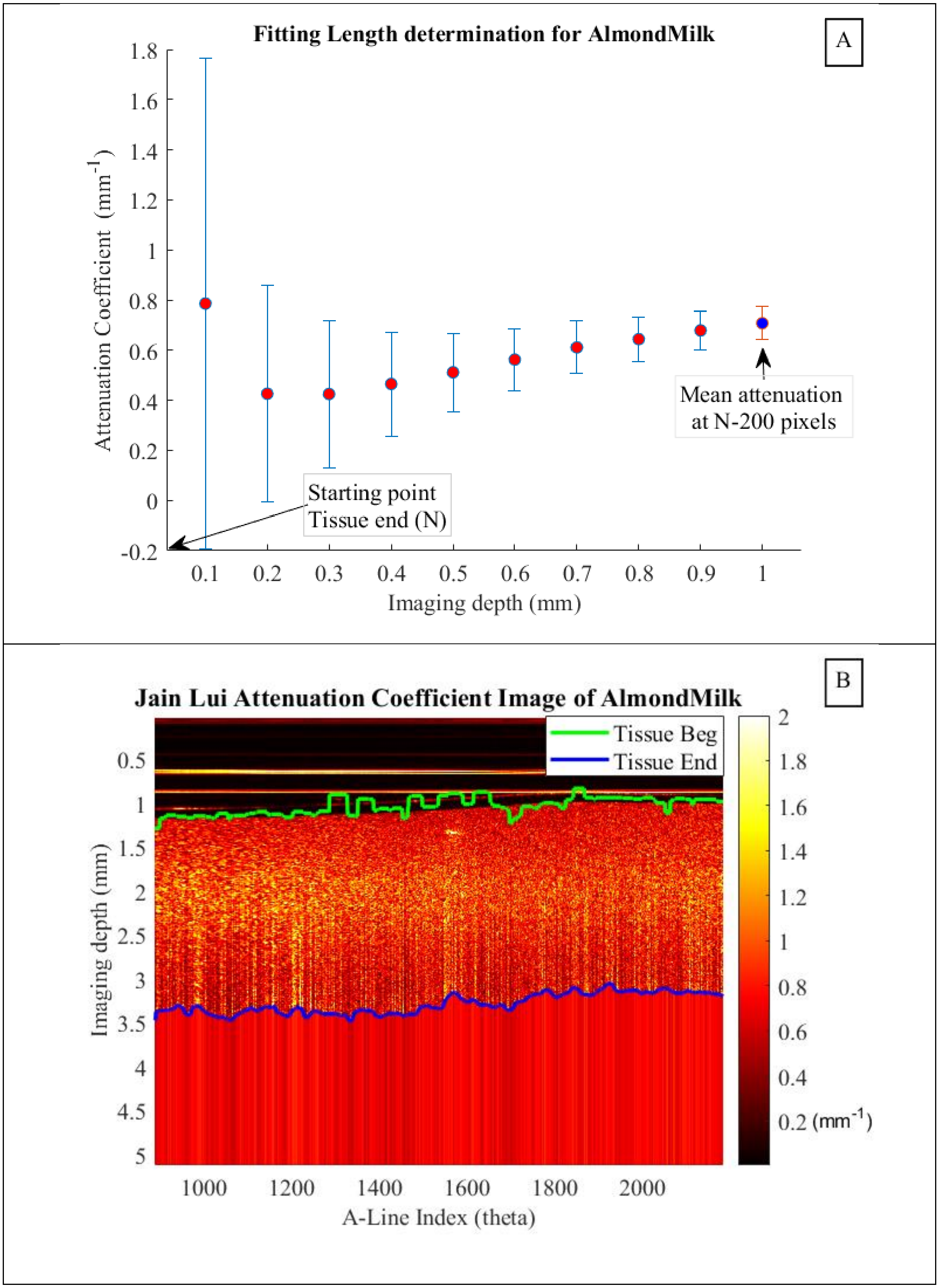

Figure 13 *(A) Fitting length determination μ[N] of almond milk. (B) Jain Lui attenuation coefficient image of a cross- sectional frame of almond milk.*

We have calculated μ[N] values for each pixel across the entire volume using Eq (9). To quantify the method's performance accurately, it is crucial to identify the tissue area. This determination is necessary to minimize the standard deviation (std). Specifically, as the beginning of the frame has zero μ[N] (Figure 13B) and the bottom has different values, averaging μ[N] for the entire frame would result in a significantly varied standard deviation. To achieve this, we need to identify the starting point of the tissue within the sample. To locate the appropriate tissue beginning, I employ series of image processing steps. I begin by using Canny edge detection to identify the tissue edges. Subsequently, I apply 2D median and Gaussian(5.5 kernel size) filters to eliminate the artifacts and speckle noise. After this, I assume the tissue is the largest connected region and identify the connected regions and discard the rest to pinpoint the tissue's starting edge, as visually depicted in Figure 14(A-D). Finally, I compute the mean attenuation coefficient of the tissue area to get a mean μ[N] for the results.

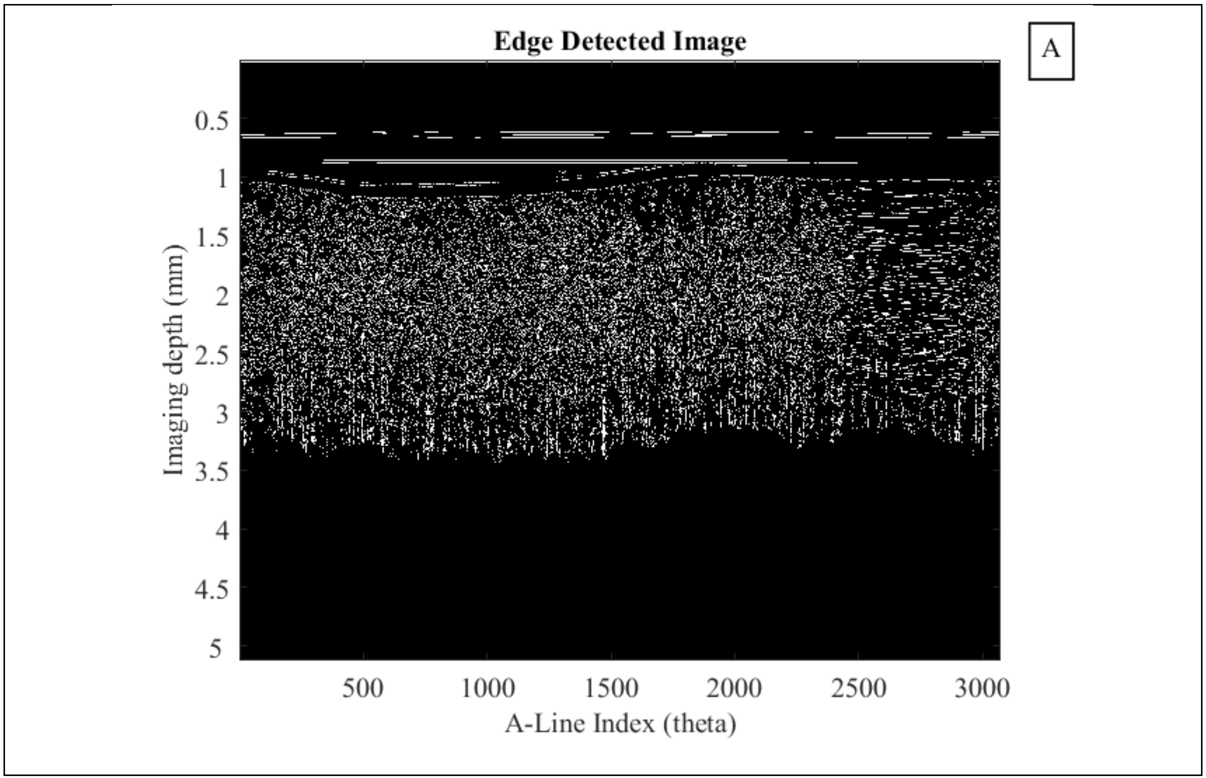

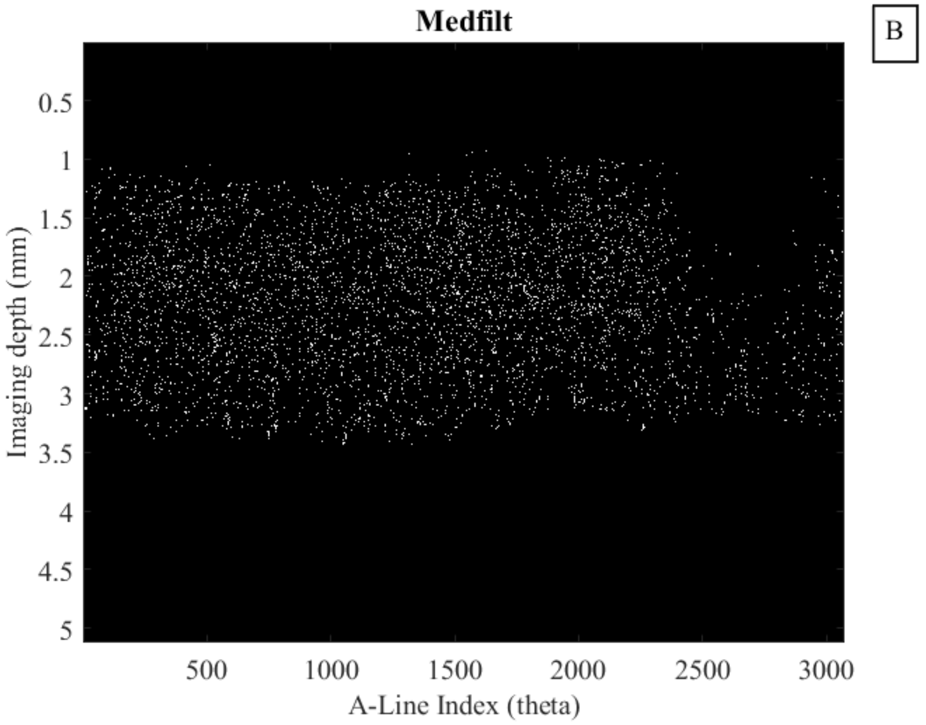
Medfilt

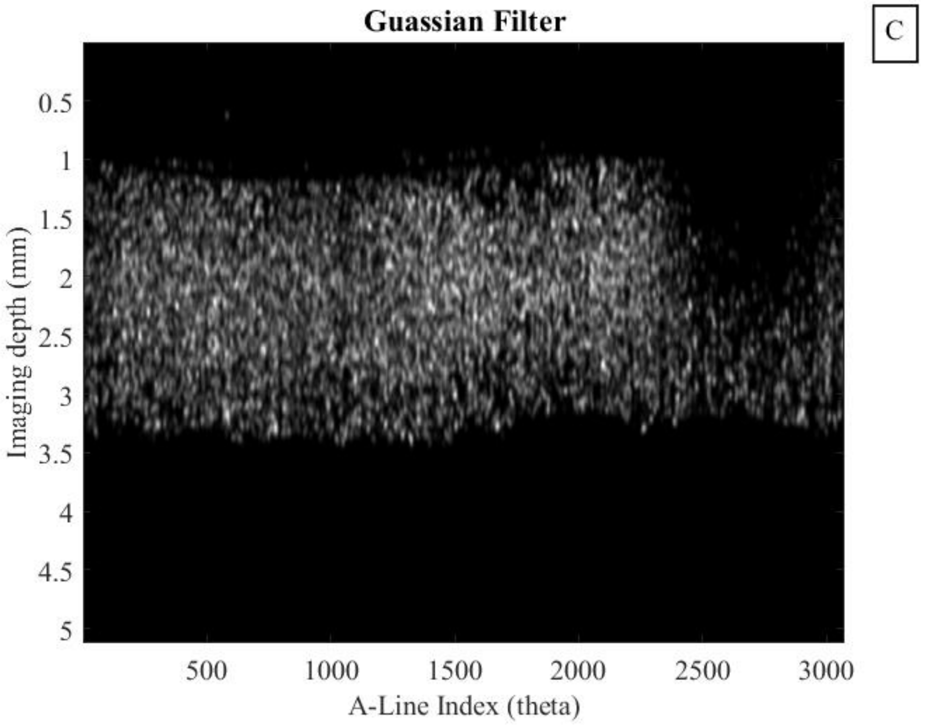
Guassian Filter

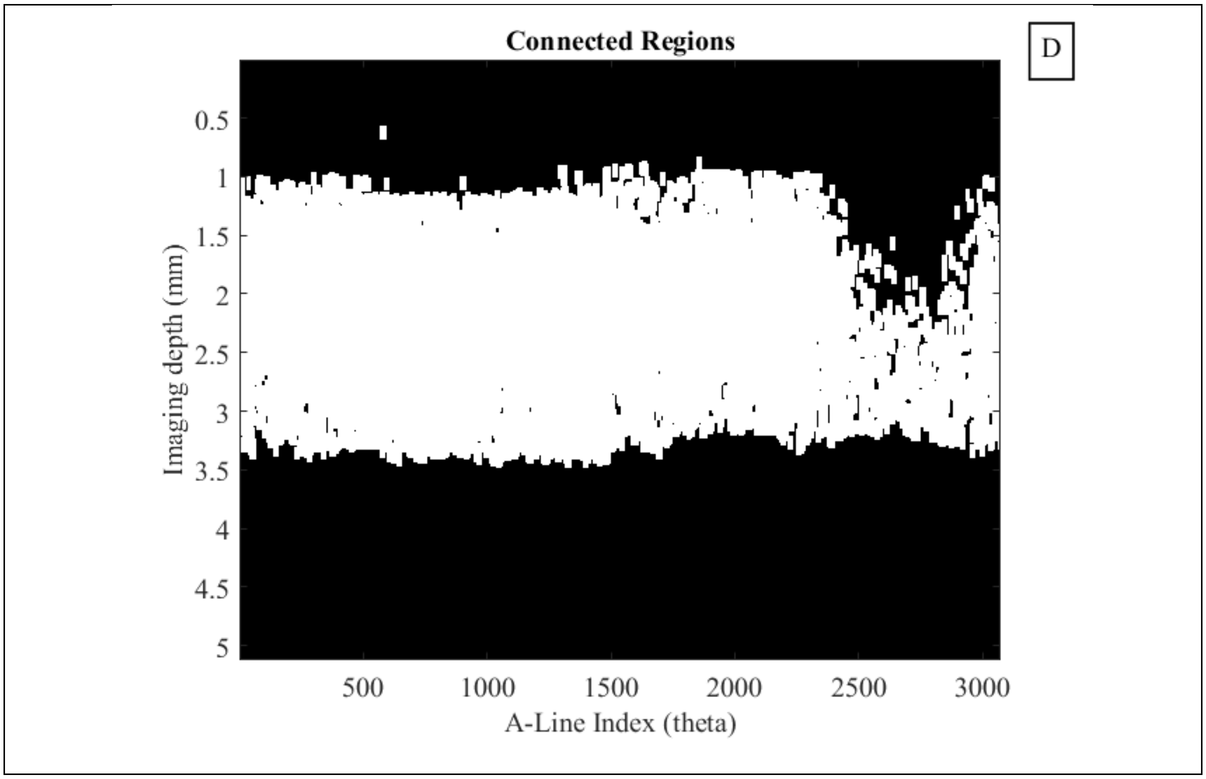

Figure 14 *(A) Edge detection applied on cross-sectional image of almond milk. (B) Median filter applied on a cross-sectional image of almond milk. (C) Gaussian filter applied on a cross-sectional image of almond milk. (D) Display of connected regions frame on a cross-sectional of almond milk.*

3.2.4 Kaiyan Li Method

The way I apply the Kaiyan Li method is quite similar to how we use the Jain Lui method, particularly up to the pre-processing stage. But there is a significant change when it comes to computing the attenuation coefficient. In Kaiyan Li, I calculate it recursively, and it is determined for each pixel, not per A-line. I use 4 iterations to calculate the attenuation coefficient (Figure 15A), which is the determined number of steps required for the mean μ[N] calculated by the algorithm to converge as we observe in Figure 15B. Figure 16 illustrates the summary of the implementation of all the four algorithms in the form of a flow chart.

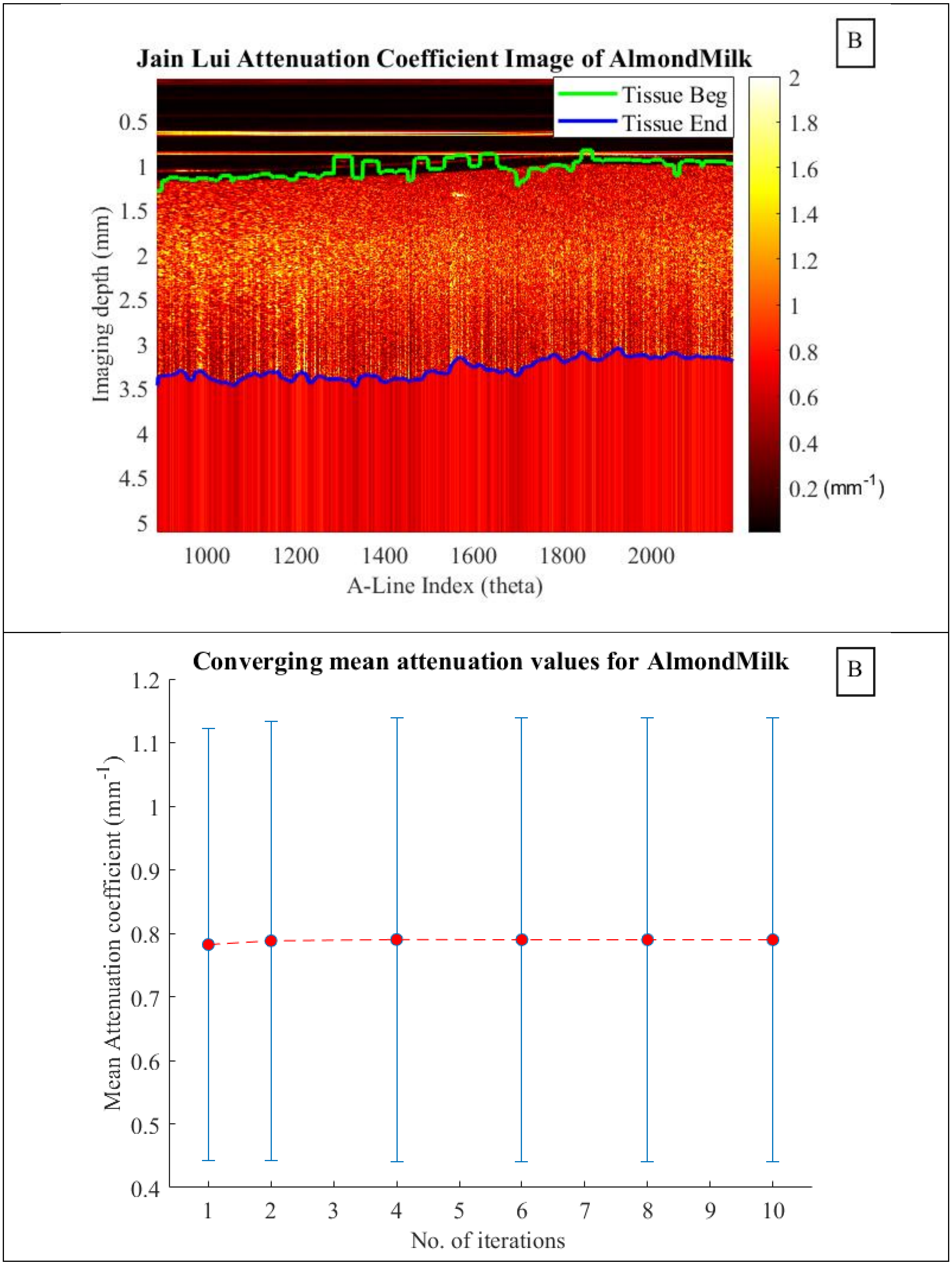

Figure 15 *(A) Kaiyan Li attenuation coefficient of a cross-sectional image of almond milk. (B) Converging attenuation values of a cross-sectional image of almond milk.*

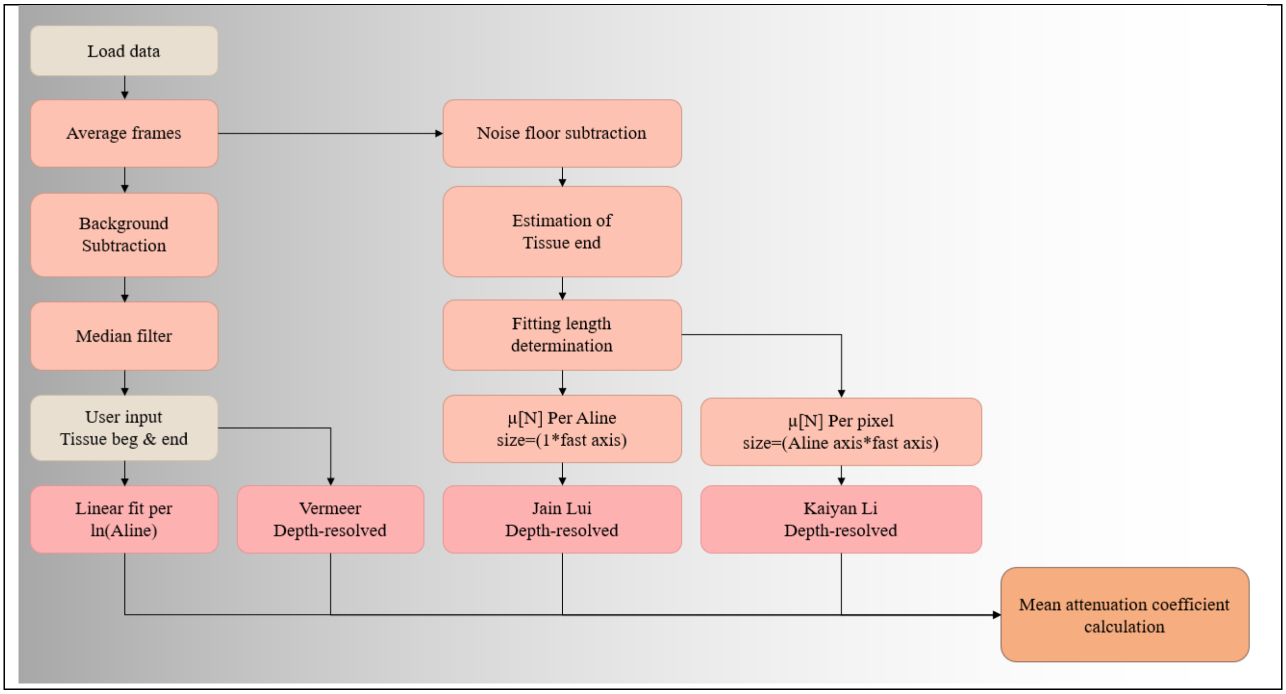

Figure 16 *Summarized flow chart of the four algorithms.*

3.3 Validation Experiment

To validate the four algorithms, I conducted an experiment using varying intralipid concentrations. In this experiment, I simultaneously assessed the attenuation coefficient through two methods: one by measuring the intensity change as light it transmitted through a sample and the other by extracting the attenuation coefficient from OCT images of the same samples.

In the initial part of the experiment, I connected the SS-OCT system to an aspheric collimator (f=8.13 mm) using an optical fiber. I allowed a 1310 nm light to pass through the collimator and transverse through an aspherical lens with the focal length of 7.50 mm. This light interacted with the concentration sample of intralipid contained within 2mm length cuvette and returned as backscattered light through the same optical path, as depicted in Figure 17A. Subsequently, I recorded the OCT signal of each concentration.

For the second part of the experiment, I maintained the same intralipid sample concentration at each increment, but removed the focusing lens and directed the collimated beam through sample. In this case, I measured the intensity of the light at the detector, as shown in Figure 17B. Afterwards I calculated the attenuation coefficient of each sample using Eq (12) [30].

$$\mu_{Sample} = \frac{1}{d}\left(\frac{Intensity_{\,water} - Intensity_{\,dark}}{Intensity_{\,Sample} - Intensity_{\,dark}}\right) \qquad \text{Eq (12)}$$

Where d is the thickness of the cuvette which is 2mm in our experiment and $Intensity_{\,dark}$ is the intensity at the detector with the laser turned off .

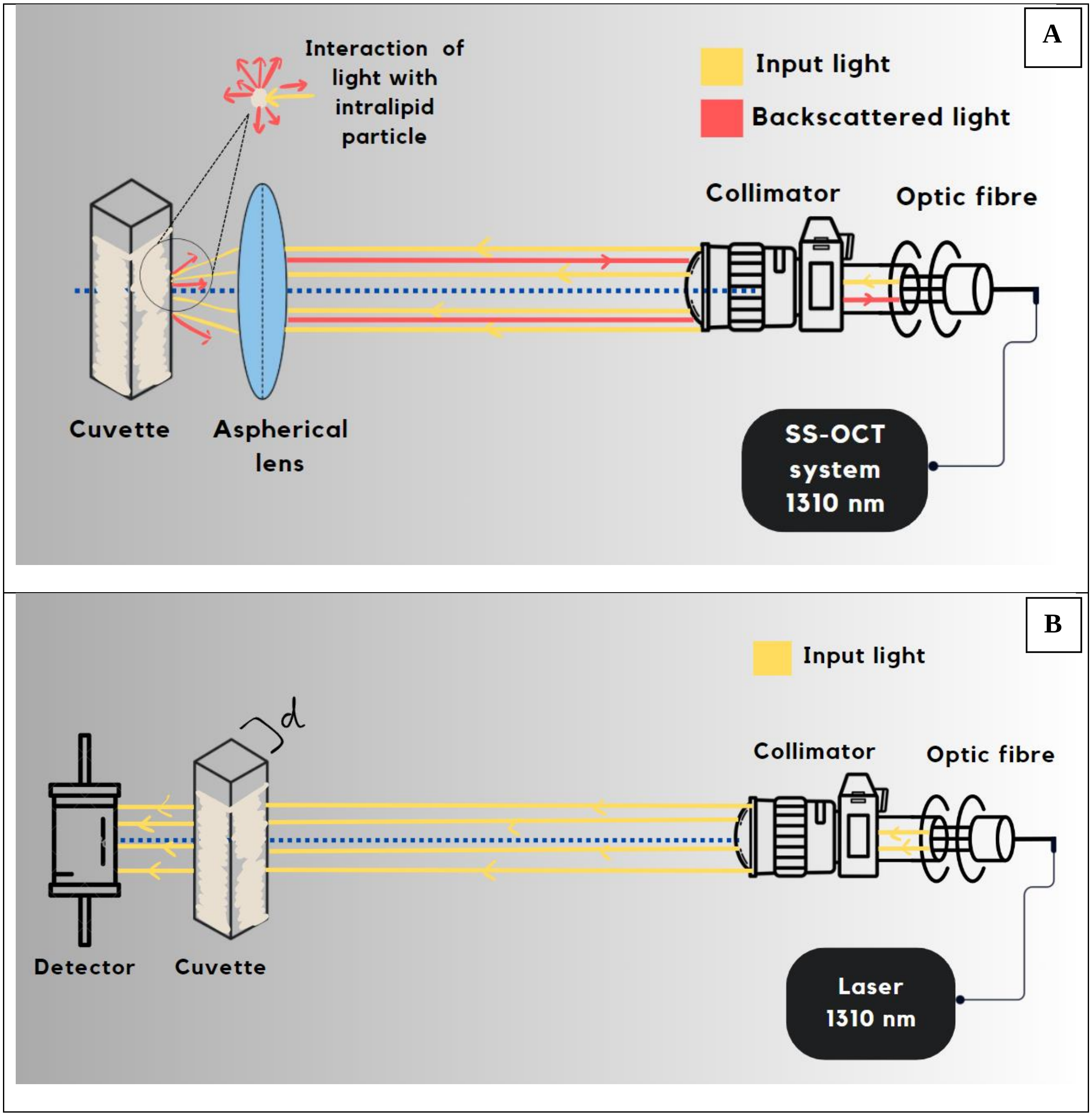

Figure 17 *(A) Optical path of the validation experiment for acquisition of the OCT signal of the intralipid samples. (B) Optical path for the acquisition of the attenuation coefficient for different intralipid samples.*

3.4 *In Vivo* samples

Lastly, the depth resolved attenuation coefficients of two OCT images from a previous *in vivo* study were computed [29]. Both images are from the same patient and taken subsequently. One side exhibited oral cancer (histologically diagnosed Dysplasia grade 3), while the contralateral side served as a normal control. To conduct a thorough analysis of the *in vivo* sample volumes, we selected the Jain Lui method due to its demonstrated accuracy and computational efficiency in Chapter 4. Due to processing limitations, cross- sectional frames around a region of interest on each sample were selected for computation. The pre-processing steps mirrored those previously discussed for the Jain Lui method (Section 3.2.3).

Unlike the intralipid and milk images, I do not generate a single mean attenuation coefficient value for the *in vivo* samples. Instead, I generate two types of images for each sample: longitudinal and *en face* (images created by performing a mean intensity projection (MIP) in the A-line direction). In working with a 3D volume, it is essential to utilize the extensive information it holds to gain a comprehensive understanding of the captured data. Although the dataset encompasses three dimensions, it is neither feasible nor practical to display every individual cross-sectional images. Instead, we turn to the concept of representative images that provide a condensed yet comprehensive view of the 3D volume. This selection is where *en face* images created from MIP on A-lines images comes into play, offering an alternative perspective that allows us to explore the dataset from a different dimension. I conducted a comparative analysis of the two image sets: the longitudinal images and the *en face* images.

Chapter 4 Results

In this section I present the outcome of our research, divided into three distinct segments. Firstly, I present the outcomes of implementing four different algorithms using milk images. Subsequently, I delve into the validation experiment conducted to assess these algorithms. Finally, I will present the findings derived from the analysis of *in vivo* images using selective pair of algorithms mentioned in Section 3.4.

4.1 Algorithm implementation using milk images

To visually represent our findings, Figure 18 depicts graphical representations of the attenuation coefficient values for the milk samples, while Table 1 provides a tabulated format for easy reference.

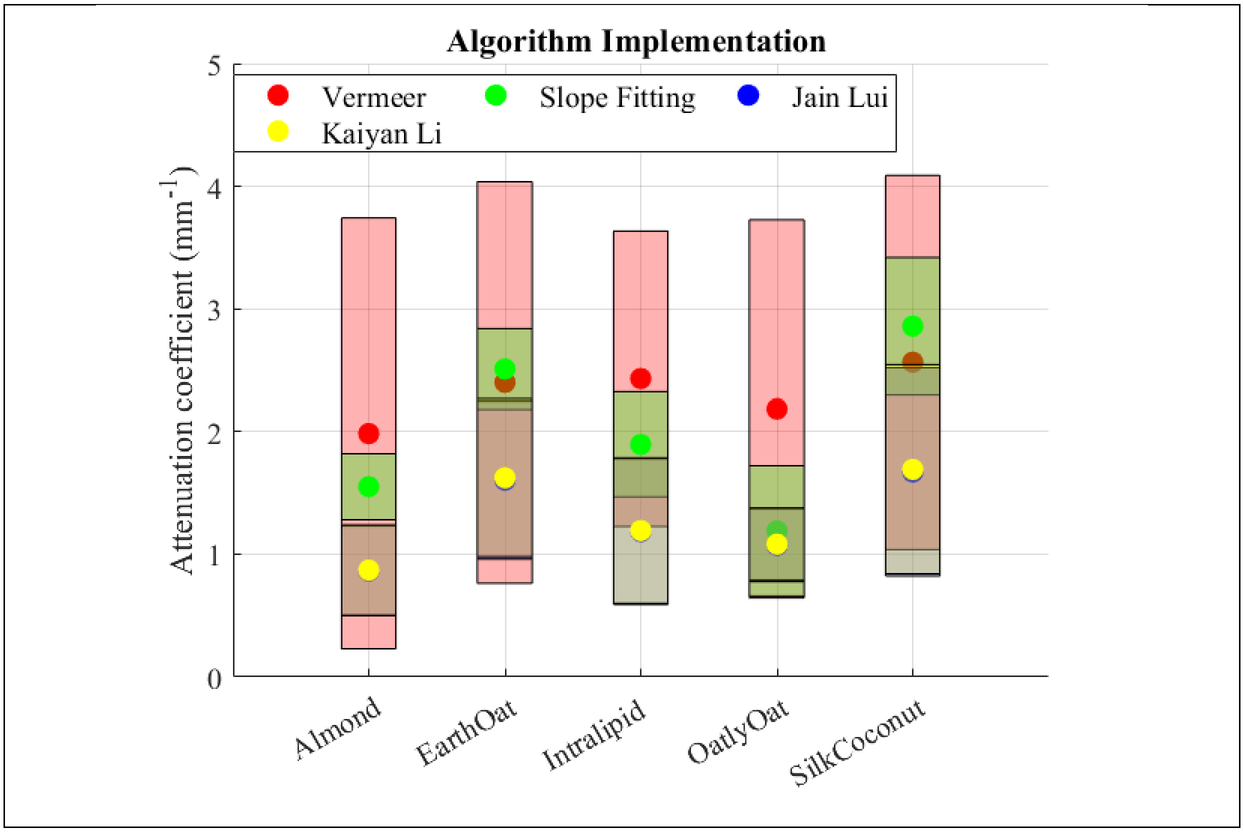

Figure 18 *Graphical representation of mean attenuation coefficient values for milk samples.*

Table 1 *Tabulated representation of mean attenuation coefficient values for milk samples.*

Milk Samples	Depth-resolved attenuation coefficient values (mm^{-1})							
	Vermeer		Slope Fitting		Jain Lui		Kaiyan Li	
	Mean	STD	Mean	STD	Mean	STD	Mean	STD
Almond	1.9844	1.7574	1.5505	0.2700	0.8632	0.3670	0.8691	0.3670
Earth Oat	2.3990	1.6382	2.5091	0.3293	1.6030	0.6435	1.6227	0.6435

Intralipid	2.4302	1.2052	1.8955	0.4285	1.1835	0.5949	1.1920	0.5949
OatlyOat	2.1848	1.5427	1.1890	0.5320	1.0722	0.2968	1.0811	0.2968
Silk Coconut	2.5637	1.5262	2.8580	0.5612	1.6701	0.8486	1.6921	0.8486

Vermeer’s method consistently generated higher attenuation coefficient values for most milk samples when compared to the other methods we employed. This observation was accompanied by a higher standard deviation in the results.

The tendency of the Vermeer method to produce these higher values can be attributed to a fundamental assumption within the method itself. The Vermeer method assumes that all incident light is entirely attenuated within the imaging depth range, denoted as I(N)=0 [25]. While this assumption holds true for scenarios with small imaging depths, we observe an exponential increase as the imaging depth increases and becomes closer to the noise floor (as discussed shortly). This phenomenon is visually depicted in Figure 11B.

The slope fitting method generally provided attenuation values between those of the Vermeer and Jain Lui methods, especially in samples with low attenuation coefficients and deeper imaging depths such as almond milk and Oatly oat barista. This phenomenon can be primarily attributed to the confocal effect, a topic that will be thoroughly expounded upon in the subsequent discussion section.

The Jain Lui and Kaiyan Li methods consistently yield depth-resolved attenuation coefficients that are notably lower, and exhibit reduced standard deviations when compared to other methods. Their calculated values tend to cluster within the lower standard deviation range of the Vermeer method. This discrepancy, where we substantially underestimate the attenuation using the Jain Lui and Kaiyan Li methods, can be attributed to the confocal effect. In the case of the Vermeer method, the response tends to approach relatively large values, largely due to the proximity of the measured values to the noise floor. However, with the Jain Lui and Kaiyan Li methods, our quantification approach is different. Towards the later stages of the sample, the confocal effect becomes more pronounced, resulting in the measurement of lower attenuation coefficients at the sample's bottom by these methods.

4.2Validation experiment

Figure 19 depicts graphical representations of the attenuation coefficient values for the intralipid samples alongside the experimental attenuation coefficient values, while Table 2 provides a tabulated format for easy reference.

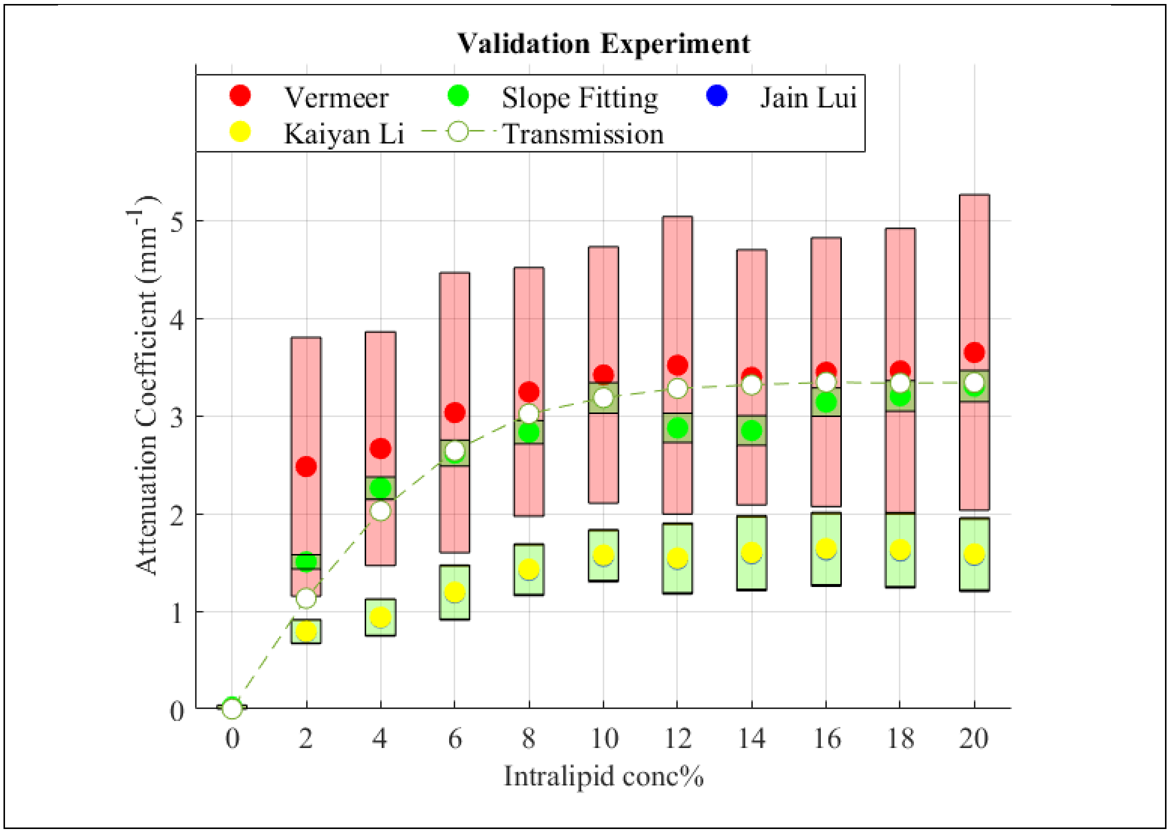

Figure 19 *Graphical representation of mean attenuation coefficient values for intralipid samples.*

Table 2 *Tabulated representation of mean attenuation coefficient values for intralipid samples.*

Intralipid Conc%	Mean depth-resolved attenuation coefficient values (mm^{-1})				
	Vermeer	Slope Fitting	Jain Lui	Kiayan Li	Experimental
0	0.0032	0.0169	0.0000	0.0000	0.0000
2	2.4759	1.5032	0.7856	0.7917	1.1304
4	2.6610	2.2556	0.9301	0.9362	2.0271
6	3.0294	2.6144	1.1842	1.1944	2.6393
8	3.2413	2.8283	1.4155	1.4290	3.0170
10	3.4157	3.1804	1.5597	1.5746	3.1821
12	3.5150	2.8721	1.5292	1.5440	3.2778
14	3.3911	2.8454	1.5852	1.6005	3.3141
16	3.4443	3.1368	1.6248	1.6411	3.3409
18	3.4568	3.2017	1.6140	1.6301	3.3318
20	3.6459	3.3012	1.5705	1.5854	3.3390

Through our validation experiment, several significant observations have emerged, shedding light on the behaviour of attenuation coefficients in response to varying intralipid concentrations. We have noticed clear trend where in the attenuation coefficient steadily increases as the percentage of intralipid in the samples increases. This trend is attributed to the heightened scattering of light and a decrease in detected power at the sensor with increasing intralipid concentration.

Another noteworthy finding is that the attenuation values tend to saturate after reaching a 10% intralipid concentration. Furthermore, as the attenuation coefficient increase, we have observed that the experiment values tend to align more closely with the results obtained using the Vermeer and Slope fitting methods.

The validation experiment aimed to measure the attenuation coefficient in transmission, establishing it as a gold standard for comparing the four OCT methods. Considering the transmission values as correct attenuation coefficient values, it is evident that the Vermeer method tends to overestimate significantly at lower concentrations and underestimate at higher concentrations of intralipid samples. In contrast, the slope fitting method emerges as the closest to the experimental values among all methods. Additionally, Jain Lui and Kaiyan Li methods generally underestimate, although for lower concentrations of intralipid, they are closer to the experimental values compared to higher concentrations.

The observed pattern from the validation experiment in Figure 19 aligns with the trends noted in our previous results in Section 4.1, where the Vermeer method consistently overestimated depth-resolved attenuation coefficient values, and the Jian Lui and Kaiyan Li methods produced lower attenuation coefficients with lower standard deviations. This behaviour may be attributed to various factors, such as imaging depth, noise floor truncation and the confocal effect, which affect the calculation of depth-resolved attenuation coefficients. A more comprehensive discussion of these factors is provided in the subsequent discussion section of this document.

From the insights gained through this validation experiment, it becomes evident that the Vermeer method exhibits a tendency to overestimate attenuation coefficients and is highly sensitive to factors like noise floor and speckle noise, similar to the slope fitting method. In light of this, we can reasonably conclude that the Jain Lui and Kaiyan Li methods offer more robust and accurate approach for calculating depth-resolved attenuation coefficients. Although both Jain Lui and Kiayan Li produce similar results, it is important to note that Kaiyan Li is computationally more intensive since it calculates the attenuation coefficient μ[N] per pixel rather than per A-line (Section 3.2.4). Therefore, Jain Lui emerges as a favourable choice providing both accuracy and computational efficiency.

4.3 *In vivo* observations

The clinical images I examined was acquired from the same patient, captured sequentially during the examination. Notably, one side of the oral cavity served as a normal control (Figure 20A), while the contralateral side exhibited a case of oral cancer, histologically diagnosed as Dysplasia grade 3 (Figure 20B).

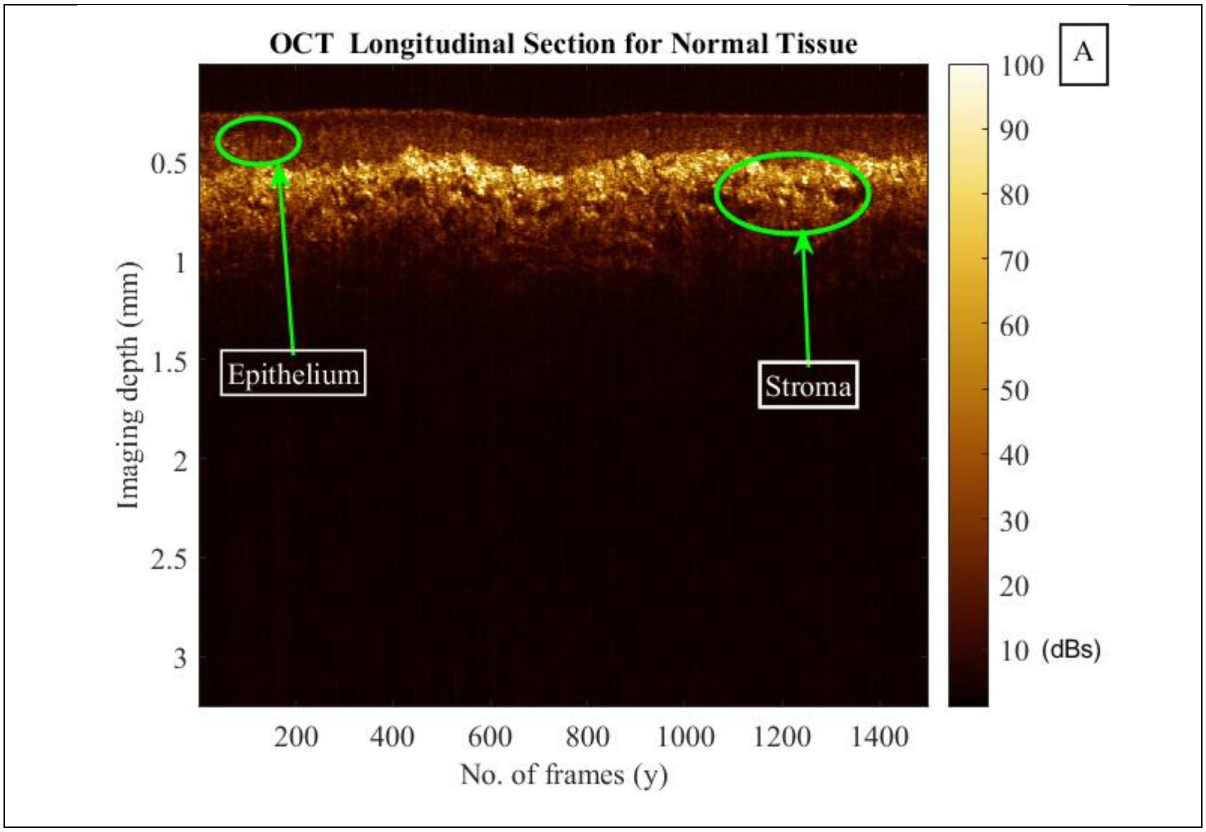
OCT Longitudinal Section for Normal Tissue
A
Epithelium
Stroma
Imaging depth (mm)
0.5
1
1.5
2
2.5
3
200
400
600
800
1000
1200
1400
No. of frames (y)
100
90
80
70
60
50
40
30
20
10 (dBs)

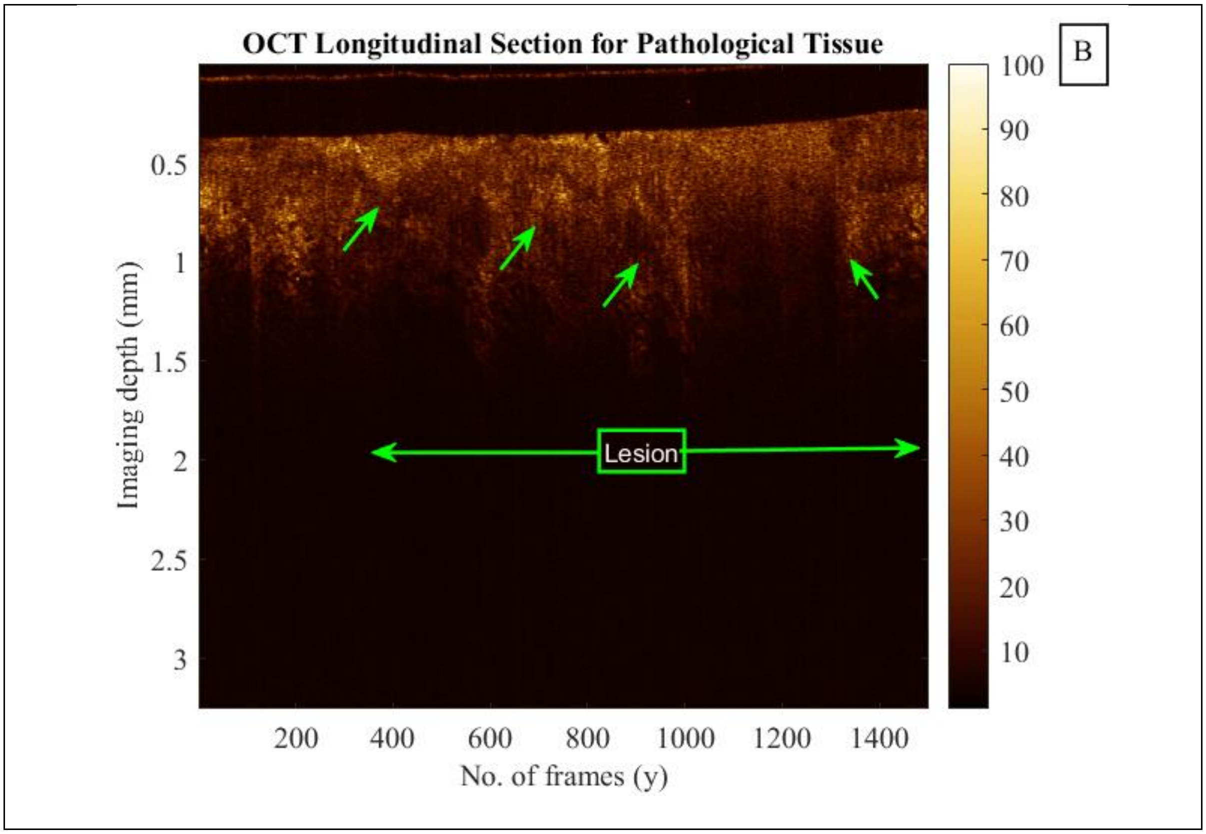

Figure 20 *(A) OCT longitudinal section of normal oral tissue. (B) OCT longitudinal section of cancerous oral tissue.*

In Figure 20A, a clear distinction is evident between the two layers of the oral cavity, namely the epithelium and the stroma. However, in the cancerous tissue, an observable alteration occurs with the stroma layer appearing mostly absent due to the presence of cancer. OCT alone allows for visualization of changes in tissue stratification associated with cancer progression, however it provides only a qualitative observation with regards to changes in tissue scattering.

Following the application of the Jain Lui method on the oral OCT images, the distinction between the two layers becomes even more apparent. Figure 21 clearly illustrates this differentiation, with the highlighted green lesion area in Figure 21B indicating the corruption of the stroma layer. In the normal tissue, strong scattering is observed in the stroma layer, marked by higher attenuation coefficients. In contrast, the same region in the cancerous tissue exhibits a lower attenuation coefficient, underscoring the marked difference in tissue characteristic between normal and cancerous states.

For instance, upon observation of both Figure 21 A and B, it is evident that there is a stromal layer present. However, when utilizing attenuation coefficient OCT, we discern a decrease in attenuation within the stromal layer of the cancerous sample. This observation may be attributed to tissue remodeling induced by cancer, wherein alterations to the extracellular matrix and surrounding tissue influence the scattering properties of light as it interacts with the modified tissue structure.

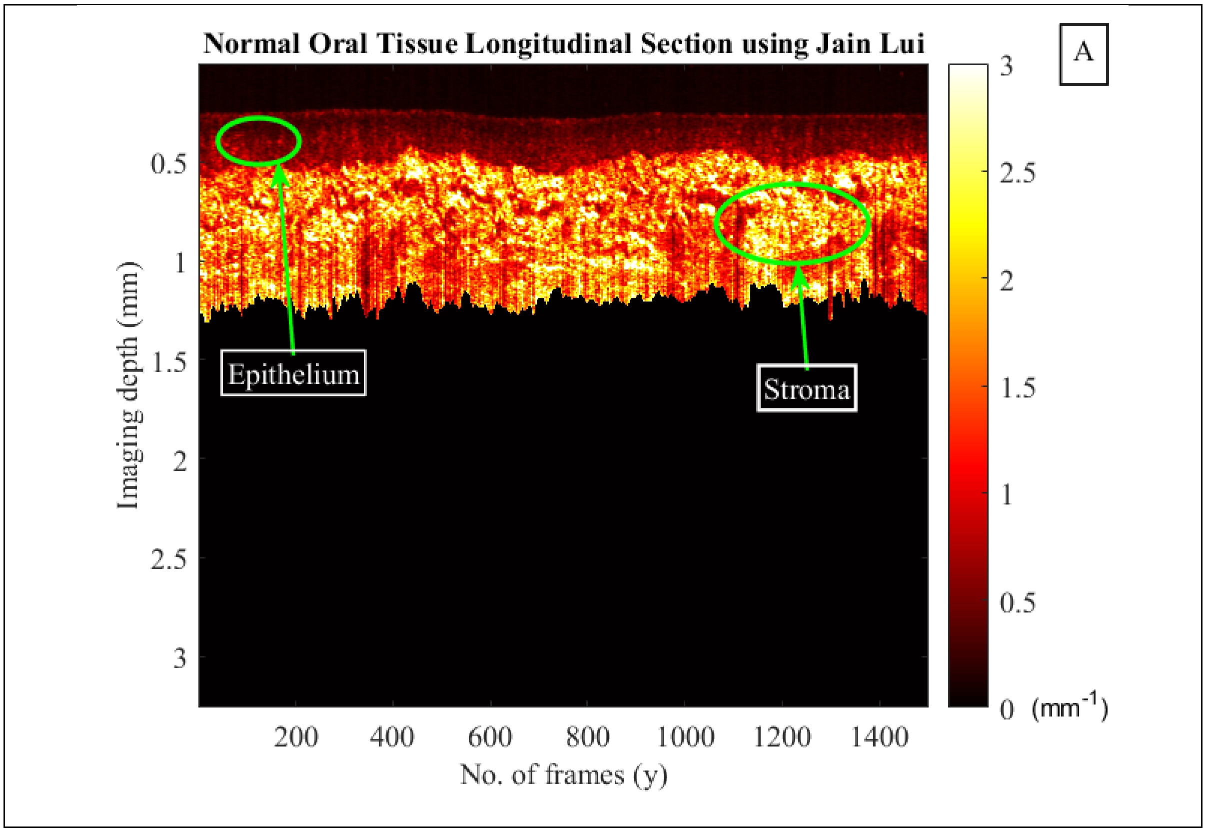

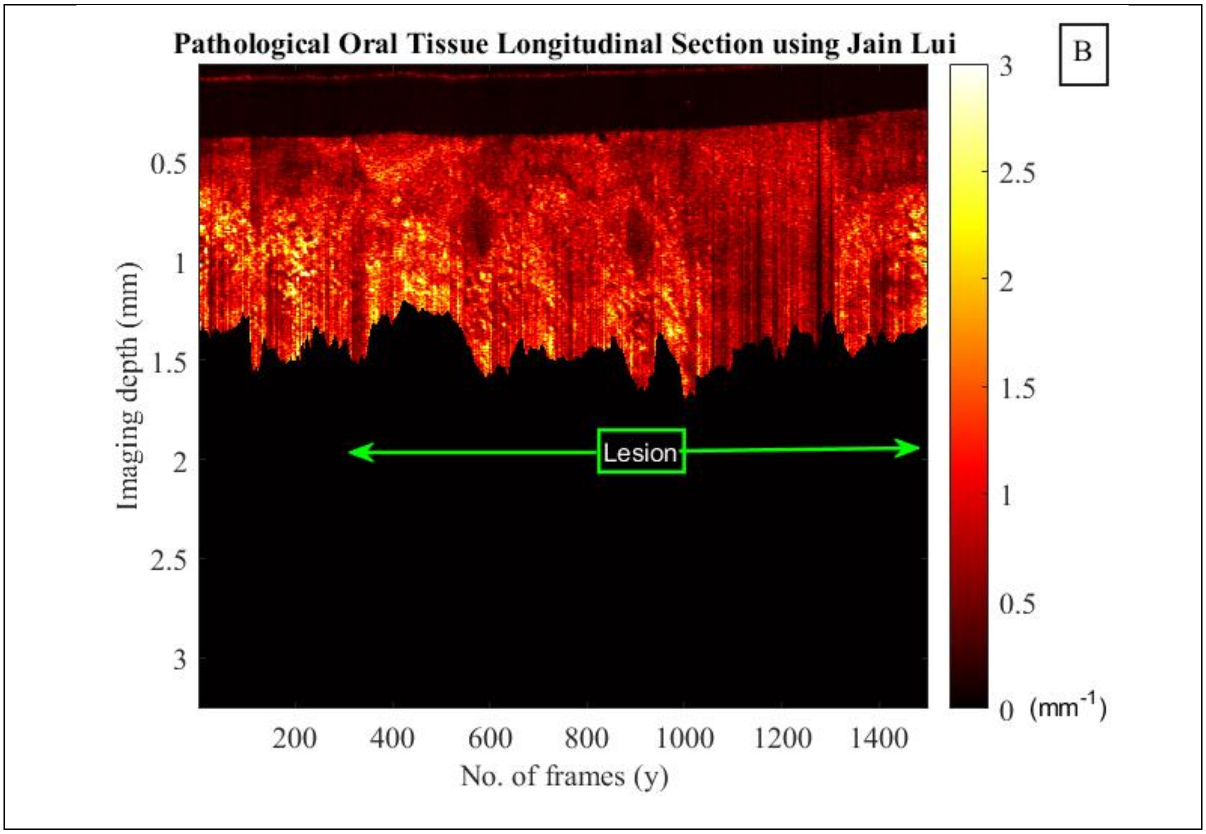

Figure 21 *(A) Attenuation coefficient longitudinal section of normal oral tissue. (B) Attenuation coefficient longitudinal section of cancerous oral tissue.*

One notable aspect of the attenuation algorithm is its ability to go beyond merely highlighting differences within cross-sectional or longitudinal frames. Upon examination of the OCT cross-sectional images in Figure 20, we observe a clear degradation of stromal layer which further seems to cause change in *en face* images. Take, for instance, Figure 22A, where the MIP of a normal tissue reveals the average of two layers: epithelium (pink arrows) and stroma (blue arrows). Interestingly, the epithelium layer is found only near the edges because the light entering the tissue at an angle is unable to read the stroma layer due to flat surface of the catheters. Notably, the high scattering values recorded in the middle area is due to the stromal layer dominating the mean attenuation coefficient.

However, this distinction becomes blurred in the cancerous tissue, as depicted in Figure 22B. The stroma layer undergoes noticeable degradation, as suggested by the altered appearance of the green arrows, and the blue circle (Figure 21B) may highlight the regions where traces of stroma still persist.

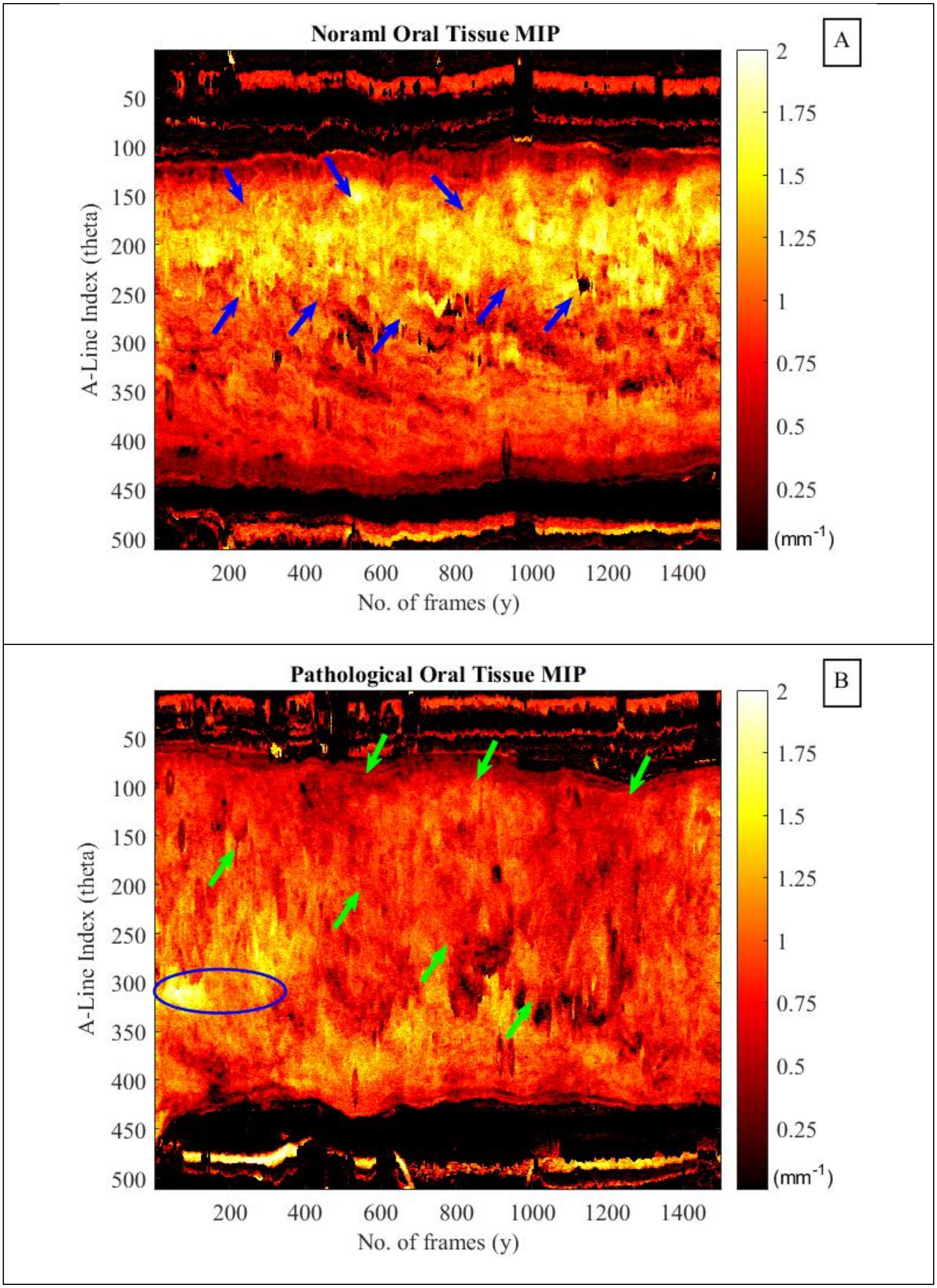

Figure 22 *(A) Attenuation coefficient MIP of normal oral tissue. (B) Attenuation coefficient MIP of cancerous oral tissue*

Chapter 5 Discussions

In this section, I commence by comparing the composition of milk samples and their literature values to the attenuation coefficients produced by our algorithm. The discussion encompasses the crucial role of pre-processing, noise floor and confocal effect with respect to the performance of the four methods used for the estimation of attenuation coefficient stated in our study. We will explore the implications of the validation experiment, the strengths and shortcomings of each method. Lastly, we will conclude by discussing potential directions for future research and applications.

5.1 Milk sample composition and attenuation coefficient correlation

The attenuation coefficient values presented in the table hold significant implications for our understanding of the properties of different milk samples. Attenuation coefficients are closely related to the milk's inherent optical properties which are indicative of the milk's composition including fat content and particle size distribution [31]. Table 3 provides data on the milk composition percentages utilized in a nutritional guide [32].

Table 3 *Milk nutrition chart (Nutrition values is per cup).*

Milk Samples	Carbs(g)	Protein (g)	Fat (g)	Saturated Fat (g)
Almond	1	1	2.5	0
Coconut	1	0	4	3.5
Earth Oat (Normal)	24	4	2.5	0
Oatly Oat (Barista)	27	4	4	3
Soybean(Intralipid)	4	7	4	0.5

Upon examining the milk sample compositions in Table 3 and the general trend of all the attenuation coefficient values shown in Figure 18, a discernible relationship becomes apparent. Higher attenuation coefficients appear to signify greater light scattering, potentially linked to larger or denser particles within the milk. Conversely, lower attenuation coefficients may point to heightened absorption, likely due to components like fat or protein. This trend is notably exemplified in the case of normal and barista oat milk, with the latter being distinguished by its higher fat content [33].

5.2 Role of pre-processing

Pre-processing plays an important role in the implementation of all of the four methods. For example, averaging of the cross-sectional images before implementing any background subtraction or noise floor reduction, significantly enhances data quality and improves the SNR (Figure 8 (A) Original and Averaged Images *of a cross sectional frame of almond milk. (B) Background subtracted and median filter images of a cross sectional frame of almond milk. Units for the* *color bar are in* A). Significantly, the slope fitting method exhibits a high degree of sensitivity to speckle noise, as it hinges on the curve fitting of OCT intensity values (Figure 10). The presence of speckle noise can profoundly affect the accuracy of the slope fitting method. However, we have observed that implementing pre-processing procedures, such as background subtraction and median filtering (Figure 8B), can markedly enhance the precision of the attenuation coefficient estimation.

5.3 Effect of noise floor

In practical scenarios, the noise floor becomes notably prominent at greater imaging depths, primarily due to the presence of multiple scattered photons and system-related noise. This results in the informative signal rapidly diminishing and converging with the noise floor, as illustrated by Figure 23 [26]. Figure 23 depicts a plot of a single A-line spanning the imaging depth for Earths Own Oat milk sample. Here, z represents the informative depth (imaging depth), N signifies the signal level above the 6dB noise floor, beyond which the signal gradually fades into the noise floor, and Tz denotes the total imaging depth of the OCT system.

The noise floor factor presents a substantial concern common to all four methods. Neglecting the consideration of the noise floor within these methods can result in either an overestimation or underestimation of the attenuation coefficient. In the case of the slope fitting method, segmentation of the tissue beginning, and tissue end is employed to eliminate the noise floor (Figure 10). However, when it comes to the Vermeer method, there are additional complexities at play that require further considerations.

In scenarios involving shallow depth samples, where z is significantly smaller than N one might naturally consider the possibility that Tz approaches infinity ($Tz=\infty$) [26]. However, it's essential to recognize that this assumption tends to lead to the underestimation of the attenuation coefficient, as can be clearly observed in Figure 18. In this figure, we can see that samples characterized by both higher attenuation coefficients and shallow imaging depths, such as Earth's Own Oat and intralipid, display pronounced underestimations of their attenuation coefficients. Moreover, Figure 19 reinforces this observed trend, especially when dealing with higher intralipid concentrations. In such cases, the underestimation of the attenuation coefficients remains a consistent feature.

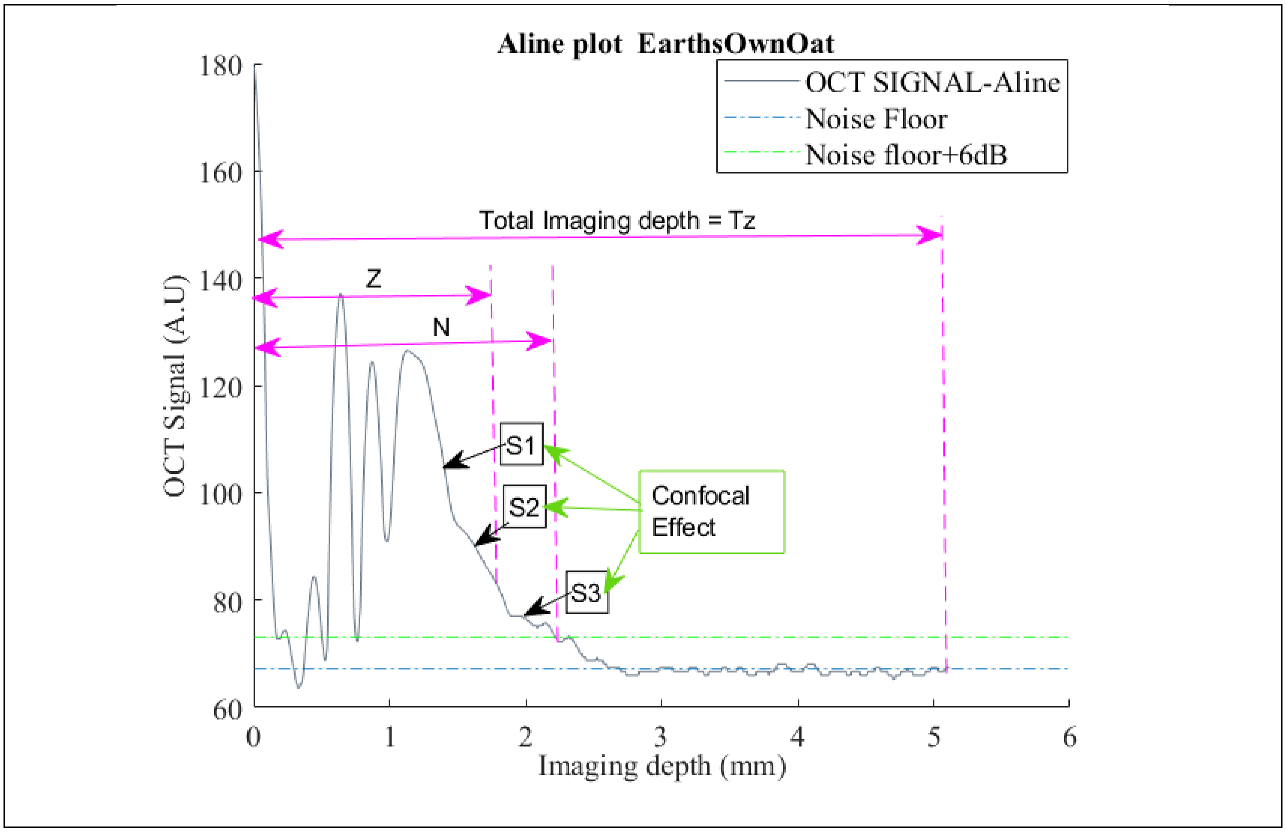

Figure 23 *A-line plot for Earths Own Oat milk sample.*

When we decide to remove the noise floor in an effort to prevent underestimation, we effectively bring z closer to N However, this adjustment leads to a violation of the assumption that all incident light is fully attenuated within the imaging depth [26]. Consequently, this deviation results in the overestimation of the attenuation coefficient, a trend that is clearly evident in samples characterized by larger imaging depths and lower attenuation coefficients, as exemplified by Almond milk and Oatly oat barista in Figure 18. Furthermore, this observed trend persists in Figure 19, particularly in the case of lower concentrations of intralipid samples, where the overestimation of attenuation coefficients is particularly pronounced.

Conversely, the Jian Lui and Kaiyan Li methods offer a remedy for the inherent tendency of the Vermeer method to yield higher values as the signal approaches the noise floor. Both of these methods accomplish this correction by approximating the attenuation coefficient value (μ[N]) through a slope fit, for the signal occurring at 6dB above the noise floor, as depicted in Figure 13A.

5.4 Confocal effect

The confocal effect (Figure 23) is a critical factor that none of the four algorithms consider during their calculations. This effect becomes particularly pronounced in samples characterized by lower attenuation coefficients, as they entail deeper sample depths. When operating far from the focal point of the optics, changes in intensity occur due to the confocal effect of the lens, which can be effectively modeled by a shift in the magnitude of the axial point spread function. As we extend our observations away from the focal point, we notice changes in the intensity response, resulting in more significant deviations from the actual values. For instance, in Figure 23, Earth's own oat is traditionally expected to demonstrate a uniform attenuation profile (uniform slope). However, upon plotting an A-line we observe distinct slope changes labeled as S1, S2 and S3 at various locations along the A-line. These deviations contribute to the underestimation of attenuation coefficients, especially in samples characterized by low attenuation coefficients and greater imaging depths. The confocal effect exerts its most pronounced influence on the Jian Lui and Kaiyan Li methods.

In the Jian Lui and Kaiyan Li methods, as indicated by Eq (9) and Eq (10), we calculate μ[N] by fitting the slope at the end of the N signal, as depicted in Figure 23. If deviations occur at the signal's end due to the confocal effect, we inadvertently calculate an underestimated μ[N], which, in turn, leads to the underestimation of both Eq (9) and Eq (10). Consequently, this further results in the underestimation of attenuation coefficient values. This trend becomes particularly apparent in cases where lower intralipid concentrations (Figure 1Figure 19) exhibit lower attenuation coefficients with greater imaging depth, resulting in their underestimation compared to the experimental values.

5.5 Implications of validation experiment

The validation experiment demonstrated a mostly linear relationship between intralipid concentration and the attenuation coefficient, highlighting the impact of increased scattering with higher concentration Figure 19. Another noteworthy finding is that the attenuation values tend to saturate after reaching a 10% intralipid concentration. This saturation occurs as the individual scattering events lose their independence, giving rise to multiple scattering phenomena. This transition results in a violation of the linearity between the attenuation coefficient and concentration [30]. Moreover, this effect challenges the assumption of constant backscattering fraction (α) of backscattered attenuated light and adds complexity to the interpretation of results.

While all four methods and the experimental values generally exhibit a congruent alignment with the expected trend of attenuation coefficients in relation to intralipid concentration, certain discrepancies compared to the literature values raise concerns regarding potential sources of experimental errors. Variations in ambient room lighting can affect power measurements by introducing fluctuations in the background. However, these lighting variations do not impact OCT results, as any detected signal remains non-coherent at the detector. Furthermore, adjustments made to the cuvette's alignment during the experiment have the potential to impact power measurements, consequently influencing OCT images due to shifts in focus.

5.6 Strength and shortcomings of all methods

Our research incorporated four distinct methods each with its unique strength and weaknesses. The slope fitting method aligns closely with experimental values for uniform intralipid samples, potentially serving as a benchmark for calculating attenuation coefficients in uniformly attenuating samples. However, it requires meticulous pre-processing and manual cropping in multilayer or heterogeneous tissue further limiting its practical utility.

The Vermeer method offers a depth-resolved approach to estimating attenuation coefficients with fine resolution and without the need for prior tissue segmentation. However, it is highly sensitive to noise floor and tend to differ from real attenuation coefficient values. It consistently produced higher attenuation values as compared to the other methods with larger standard deviations.

From the insights gathered through validation experiment and considering the sensitivity to noise floor, Jain Lui and Kaiyan Li methods emerge as robust and accurate approaches for calculating depth-resolved attenuation coefficients. Conversely, Jain Lui and Kaiyan Li methods consistently generated lower depth-resolved attenuation coefficients with lower standard deviations. While both provide similar results, Kaiyan Li is computationally more intensive, making Jain Lui the favourable choice. However, none of the methods considered the confocal effect which highly altered the attenuation coefficient values especially in Jain Lui and Kiayan Li.

Chapter 6 Conclusion

6.1 Conclusion

The study delves into the exploration of OCT as a tool for early cancer diagnosis, revealing its promising attributes as a potential to aid and reduce invasive biopsies. The study focused on the calculation of the attenuation coefficient (μ) using four distinct methods: slope-fitting, Vermeer, Jain Lui and Kaiyan Li. The comprehensive comparisons involved implementation assessments on various types of milk OCT images, followed by further validation by comparison against measurements from a power meter and OCT images with various intralipid concentrations. The optimal algorithm identified through these evaluations was subsequently applied to generated OCT images for both cancerous and normal oral tissues.

A thorough examination was conducted to scrutinize the critical factors influencing the performance of the four methods. Pre-processing techniques, such as frame averaging, were identified as enhancing data quality and SNR. The effects of the noise floor and confocal effects, especially at greater imaging depths, were observed and explained comprehensively. These factors contributed to the overestimation of the Vermeer method and the underestimation of the Jain Lui and Kaiyan Li methods. Validation experiment established a linear relationship between intralipid concentration and attenuation coefficient, yet multiple scattering in higher intralipid concentrations challenged the assumption of a constant backscattering fraction.

Each method demonstrated its strength and shortcomings, underscoring the imperative for further research. The need to explicitly incorporate confocal effects and address multiple scattering emerged as critical areas for improvement in depth-resolved algorithms, with the ultimate goal of enhancing estimation of attenuation coefficient in the realm of cancer diagnostics.

6.2 Future Work

It is essential to acknowledge the existence of several promising avenues for future research that can further expand upon the findings presented in this thesis. These future studies could encompass the development of a model that explicitly incorporates the confocal effect into its calculations. Additionally, efforts to estimate the precise position of the focus in the RPC system could yield a deeper understanding of the confocal effect's impact.

Another prospective area of research involves extending the depth-resolved attenuation calculation to account for the influence of multiple scattering, thus broadening the scope of our understanding. Furthermore, there is potential for research that combines depth-resolved algorithms with advanced deep neural networking techniques, with a focus on tasks such as detecting tissue layer boundaries. Such an approach has the potential to enhance our ability to gain insights into quantitative tissue scattering characterization, and this, in turn, can have far-reaching implications for biomedical research and clinical applications.

References

[1] "Cancer." Accessed: Sep. 03, 2023. [Online]. Available: https://www.who.int/news-room/fact-sheets/detail/cancer

[2] "Clear, ultra-high-definition imagery for surgeons during surgery," Perimeter Medical. Accessed: Sep. 03, 2023. [Online]. Available: https://perimetermed.com/benefits-to-surgeons/

[3] J. G. Fujimoto, C. Pitris, S. A. Boppart, and M. E. Brezinski, "Optical Coherence Tomography: An Emerging Technology for Biomedical Imaging and Optical Biopsy," *Neoplasia N. Y. N*, vol. 2, no. 1–2, pp. 9–25, Jan. 2000.

[4] S. Lee, "Cancer statistics at a glance," Canadian Cancer Society. Accessed: Sep. 03, 2023. [Online]. Available: https://cancer.ca/en/research/cancer-statistics/cancer-statistics-at-a-glance

[5] *Oxford cancer researcher explains why cancer is so hard to cure (and what to do instead)*, (Oct. 10, 2022). Accessed: Sep. 03, 2023. [Online Video]. Available: https://www.youtube.com/watch?v=qY7-3cAMVxE

[6] D. M. Laronde, "Oral Cancer: Just the Facts," vol. 74, no. 3, 2008.

[7] "History of Cancer Screening and Early Detection: 20th Century to Present." Accessed: Sep. 03, 2023. [Online]. Available: https://www.cancer.org/cancer/understanding-cancer/history-of-cancer/screening-early-detection.html

[8] R. Hou, T. Le, S. D. Murgu, Z. Chen, and M. Brenner, "Recent advances in optical coherence tomography for the diagnoses of lung disorders," *Expert Rev. Respir. Med.*, vol. 5, no. 5, pp. 711–724, Oct. 2011, doi: 10.1586/ers.11.59.

[9] P. Gong *et al.*, "Parametric imaging of attenuation by optical coherence tomography: review of models, methods, and clinical translation," *J. Biomed. Opt.*, vol. 25, no. 4, p. 040901, Apr. 2020, doi: 10.1117/1.JBO.25.4.040901.

[10] L. D. Fiske *et al.*, "Bayesian analysis of depth resolved OCT attenuation coefficients," *Sci. Rep.*, vol. 11, no. 1, Art. no. 1, Jan. 2021, doi: 10.1038/s41598-021-81713-7.

[11] T. M. Cannon, B. E. Bouma, and N. Uribe-Patarroyo, "Layer-based, depth-resolved computation of attenuation coefficients and backscattering fractions in tissue using optical coherence tomography," *Biomed. Opt. Express*, vol. 12, no. 8, pp. 5037–5056, Aug. 2021, doi: 10.1364/BOE.427833.

[12] K. A. Vermeer, J. Mo, J. J. A. Weda, H. G. Lemij, and J. F. de Boer, "Depth-resolved model-based reconstruction of attenuation coefficients in optical coherence tomography," *Biomed. Opt. Express*, vol. 5, no. 1, pp. 322–337, Jan. 2014, doi: 10.1364/BOE.5.000322.

[13] "Experimental Validation of the Attenuation Coefficient of Bidisperse Discrete Random Media | TU Delft Repositories." Accessed: Sep. 03, 2023. [Online]. Available: https://repository.tudelft.nl/islandora/object/uuid%3A32fe1d76-8c7d-4550-95bf-f4ce1d5b1561

[14] J. A. Izatt, M. A. Choma, and A.-H. Dhalla, "Theory of Optical Coherence Tomography," in *Optical Coherence Tomography: Technology and Applications*, W. Drexler and J. G. Fujimoto, Eds., Cham: Springer International Publishing, 2015, pp. 65–94. doi: 10.1007/978-3-319-06419-2_3.

[15] S. Aumann, S. Donner, J. Fischer, and F. Müller, "Optical Coherence Tomography (OCT): Principle and Technical Realization," in *High Resolution Imaging in Microscopy and Ophthalmology: New Frontiers in Biomedical Optics*, J. F. Bille, Ed., Cham: Springer International Publishing, 2019, pp. 59–85. doi: 10.1007/978-3-030-16638-0_3.

[16] "What's the Right OCT for You?," Eyes On Eyecare. Accessed: Sep. 15, 2023. [Online]. Available: https://eyesoneyecare.com/resources/whats-the-right-oct-for-you/

[17] "OCT Tutorial," Wasatch Photonics. Accessed: Sep. 15, 2023. [Online]. Available: https://wasatchphotonics.com/oct-tutorial/

[18] U. F. O. Themes, "21 Squamous Cell Cancer of the Alveolar Ridge," Pocket Dentistry. Accessed: Sep. 03, 2023. [Online]. Available: https://pocketdentistry.com/21-squamous-cell-cancer-of-the-alveolar-ridge/

[19] H. Luo *et al.*, “Human colorectal cancer tissue assessment using optical coherence tomography catheter and deep learning,” *J. Biophotonics*, vol. 15, no. 6, p. e202100349, 2022, doi: 10.1002/jbio.202100349.

[20] S. Yazdanfar, M. D. Kulkarni, and J. A. Izatt, “High resolution imaging of in vivo cardiac dynamics using color Doppler optical coherence tomography,” *Opt. Express*, vol. 1, no. 13, pp. 424–431, Dec. 1997, doi: 10.1364/OE.1.000424.

[21] M. A. Choma, M. V. Sarunic, C. Yang, and J. A. Izatt, “Sensitivity advantage of swept source and Fourier domain optical coherence tomography,” *Opt. Express*, vol. 11, no. 18, pp. 2183–2189, Sep. 2003, doi: 10.1364/OE.11.002183.

[22] D. Huang *et al.*, “Optical Coherence Tomography,” *Science*, vol. 254, no. 5035, pp. 1178–1181, Nov. 1991.

[23] W. Drexler *et al.*, “In vivo ultrahigh-resolution optical coherence tomography,” *Opt. Lett.*, vol. 24, no. 17, pp. 1221–1223, Sep. 1999, doi: 10.1364/OL.24.001221.

[24] G. T. Smith *et al.*, “Automated, Depth-resolved Estimation of the Attenuation Coefficient From Optical Coherence Tomography Data,” *IEEE Trans. Med. Imaging*, vol. 34, no. 12, pp. 2592–2602, Dec. 2015, doi: 10.1109/TMI.2015.2450197.

[25] J. Liu *et al.*, “Optimized depth-resolved estimation to measure optical attenuation coefficients from optical coherence tomography and its application in cerebral damage determination,” *J. Biomed. Opt.*, vol. 24, no. 3, p. 035002, Mar. 2019, doi: 10.1117/1.JBO.24.3.035002.

[26] K. Li, W. Liang, Z. Yang, Y. Liang, and S. Wan, “Robust, accurate depth-resolved attenuation characterization in optical coherence tomography,” *Biomed. Opt. Express*, vol. 11, no. 2, pp. 672–687, Feb. 2020, doi: 10.1364/BOE.382493.

[27] Y. Wang, S. Wei, and J. U. Kang, “Depth-resolved backscattering signal reconstruction based OCT attenuation compensation,” in *Optical Fibers and Sensors for Medical Diagnostics, Treatment and Environmental Applications XXII*, SPIE, Mar. 2022, pp. 71–75. doi: 10.1117/12.2609114.

[28] Y. Wang, S. Wei, S. Guo, and J. U. Kang, “Optimized OCT-based depth-resolved model for attenuation compensation using point-spread-function calibration,” in *Optical Fibers and Sensors for Medical Diagnostics, Treatment and Environmental Applications XXI*, SPIE, Mar. 2021, pp. 35–40. doi: 10.1117/12.2577847.

[29] A. M. D. Lee, L. Cahill, K. Liu, C. MacAulay, C. Poh, and P. Lane, “Wide-field in vivo oral OCT imaging,” *Biomed. Opt. Express*, vol. 6, no. 7, pp. 2664–2674, Jul. 2015, doi: 10.1364/BOE.6.002664.

[30] “Total attenuation coefficient of intralipid dilutions for discrete laser wavelengths between 405 and 1315 nm.” Accessed: Oct. 26, 2023. [Online]. Available: https://www-spiedigitallibrary-org.proxy.lib.sfu.ca/conference-proceedings-of-spie/9447/1/Total-attenuation-coefficient-of-intralipid-dilutions-for-discrete-laser-wavelengths/10.1117/12.2087266.full

[31] W. R. Calhoun, H. Maeta, S. Roy, L. M. Bali, and S. Bali, “Sensitive real-time measurement of the refractive index and attenuation coefficient of milk and milk-cream mixtures,” *J. Dairy Sci.*, vol. 93, no. 8, pp. 3497–3504, Aug. 2010, doi: 10.3168/jds.2010-3045.

[32] S. S. RD, “A Nutritional Comparison of Dairy and Plant-based Milk Varieties,” MyFitnessPal Blog. Accessed: Oct. 28, 2023. [Online]. Available: https://blog.myfitnesspal.com/a-nutritional-comparison-of-dairy-and-plant-based-milk-varieties/

[33] “FAQs | Oatly US.” Accessed: Oct. 30, 2023. [Online]. Available: https://www.oatly.com/en-us/random-answers